International Journal of Material Forming (2022) 15: 64
https://doi.org/10.1007/s12289-022-01710-7

ORIGINAL RESEARCH

Validation of material models for sheet metals using new test equipment

Matthias Eder[1] · **Maximilian Gruber**[1] · **Wolfram Volk**[1]

Received: 4 May 2022 / Accepted: 8 July 2022 / Published online: 25 July 2022

Abstract

Validation is an important step after a calibration of models in order to assess their quality. In this work, new test equipment is presented that provides a comprehensive database for validation of material models for numerical analyses using FE simulation in sheet metal forming: the MUC-Test (acronym for Material Under Control). The introduced validation strategy is based on a comparison of experimental results with a numerical representation of the MUC-Test in terms of punch force and major and minor strain. The data comparison approach uses a full-field comparison over a wide range of punch stroke and thus considers the hardening behavior of the models. Extensive parameter studies are performed to investigate numerical, process and material model parameters regarding their influence on the test results. The presented validation method is applied to three materials of different material classes: The microalloyed steel HC340LA, the dual-phase steel DP590HD and the aluminum alloy AA5754. Furthermore, different material models based on the same database are compared for the DP590HD, showing the potential to identify suitable material models for specific requirements. Finally, equivalent material models based on different calibration strategies are compared. In conclusion, it is shown that the MUC-Test can be used to evaluate and compare different material models in terms of their ability to represent real material behavior in an effective and efficient way.

Keywords Sheet metal forming · Material model · Validation · Parameter study · Full-field comparison · MUC-Test

Special Symbols and Abbreviations

Symbol	Unit	Meaning
$\alpha_{1\ldots8}$	-	Parameters of the material model *Yld2000*
$\varepsilon_1, \varepsilon_2$	-	First/second principal logarithmic strain (major/minor strain)
$\dot{\varepsilon}_1, \dot{\varepsilon}_2$	s^{-1}	First/second principal logarithmic strain rate (major/minor strain rate)
$\varepsilon^p_{\mathrm{eq}}$	-	Equivalent plastic logarithmic strain
$\dot{\varepsilon}^p_{\mathrm{eq}}$	s^{-1}	Equivalent plastic logarithmic strain rate
$\dot{\varepsilon}^p_{\mathrm{eq0}}$	s^{-1}	Equivalent plastic logarithmic reference strain rate
η	-	Second isoparametric parameter
ν	-	Poisson's ratio
ξ	-	First isoparametric parameter
σ_1, σ_2	MPa	First/second principle Cauchy stress
σ_{sh}	MPa	Cauchy shear stress
σ_y	MPa	Cauchy yield stress
σ_{y0}	MPa	Cauchy reference yield stress
ALPS	-	Normalized position of second principal stress under plane strain (*Vegter06*)
BBC	-	Yield locus description according to Banabic, Balan and Comsa (2005)
BT	-	Equibiaxial tension
DP steel	-	Dual-phase steel
E	GPa	Young's modulus

✉ Matthias Eder
matthias.eder@tum.de

[1] Chair of Metal Forming and Casting, TUM School of Engineering and Design, Technical University of Munich, Walther-Meissner-Str. 4, 85748 Garching near Munich, Germany

Symbol	Unit	Meaning
f_{BD}	-	Coefficient of friction between specimen and blankholder and die
f_P	-	Coefficient of friction between specimen and punch
Exp	-	Experimentally determined
F	N	Punch force
FEM	-	Finite element method
FBI	MPa / (-)	(Normalized) equibiaxial stress (*Vegter06*)
FPS1	MPa / (-)	(Normalized) first principal stress under plane strain (*Vegter06*)
FSH	MPa / (-)	(Normalized) principal stress under pure shear (*Vegter06*)
FUN	MPa / (-)	(Normalized) first principal stress point under uniaxial tension (*Vegter06*)
h	mm	Punch stroke
Hill48	-	Yield locus description according to Hill (1948)
Inv	-	Data under investigation
m	-	Exponent for strain rate dependency model
M	-	Exponent for *Yld2000* and *BBC*
MS	s	Minimum time step for mass scaling
RBI	-	Equibiaxial anisotropy coefficient (*Vegter06*)
Ref	-	Reference data
RMS	- / N	Root mean square
RUN	-	Uniaxial anisotropy coefficient (*Vegter06*)
Sim	-	Simulatively determined
SR	-	Stress ratio
SRL	mm	Strain reference length
UT	-	Uniaxial tension
Vegter06	-	Yield locus description according to Vegter and van den Boogaard (2006)
w	- / N^{-1}	weights
w_x	mm	Punch width in the x-direction
w_y	mm	Punch width in the y-direction
Yld2000	-	Yield locus description according to Barlat (2000)
$\boldsymbol{x}$	mm	Position vector

Introduction

Virtual methods are used extensively to support the engineering process. In the field of sheet metal forming, the finite element method (FEM) is particularly widespread [1]. On the one hand, the FEM is used to investigate the producibility and the resulting product properties of sheet metal components; on the other hand, it can also be used to draw conclusions about process robustness. The quality of the reality representation determines the informative value of the virtual methods. For sheet metal forming numerically represented by a FE simulation, material modeling is a central aspect in addition to the representation of the geometry and the process parameters. Only if all these categories are modeled with sufficient accuracy and precision, are the results of the virtual method reliable. In addition, model execution time, robustness, flexibility and degree of knowledge gain are also important evaluation criteria of different models. Depending on the field of application and purpose, the models have to meet different requirements in terms of model accuracy and precision [2].

In sheet metal forming, a multitude of different models exists for describing material behavior [3], cf. Figure 1. The complexity of the models varies greatly. Flow curves, yield loci and their strain hardening behavior, strain rate dependency, forming limits due to localized necking under linear and non-linear load paths are modeled depending on the desired complexity of the model [4]. However, it is not

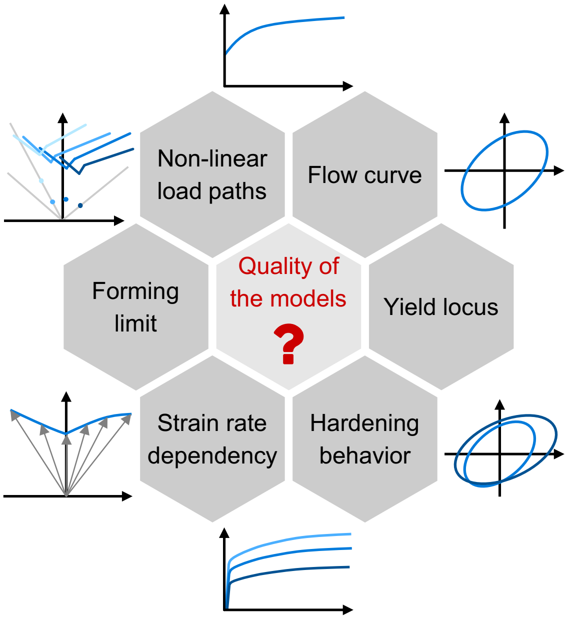

Fig. 1 Different models for describing the material behavior of sheet metals

necessarily expedient to use a model that is as complex as possible. The challenge is to find a model that is as simple as possible but sufficiently accurate [2].

The preparations for the use of material models are essentially based on two steps: first, the parameters of a model have to be calibrated. Various experiments such as tensile tests or hydraulic bulge tests are usually performed for this purpose [4]. The oscillations in the experiments as well as simplification of the assumptions in the evaluation frequently result in an uncertainty of the model parameters. Consequently, validation of the model is essential in the second step. In this way, the calibration points and, more importantly, the quality of the interpolation or extrapolation based on the model can be checked and evaluated with regard to general requirements for the model.

At present, various tests are being used in sheet metal forming to evaluate the predictive accuracy of various material models, especially yield locus models. The basic idea of the procedure is usually the same. Tests are carried out and the strains occurring on the surface of the sheets as well as the punch force are determined. Since yield loci are defined in the stress space, a direct comparison of the primary measurable quantities with the model is not possible. Therefore, a digital twin of the experiments is created using the model under investigation. FE simulation is predominantly used for this purpose. The digital twin makes it possible to generate and link measurable and model quantities. In the case of the yield locus description, the link between the stress and strain space is in the flow rule. In the present work, the associated flow rule is used throughout. The numerically determined strains on the surface of the sheet are compared with the experimentally obtained strains. If other influencing factors such as geometry and process parameters, especially friction, are sufficiently modeled, the quality of the material model used can be assessed on the basis of this comparison.

General Requirements for a Validation Test

To allow a comprehensive, effective and efficient validation of material models, it is necessary that the underlying test meets the following characteristics: for a comprehensive validation of material models, it should be possible to acquire data over the entire test sequence, so that the strain hardening behavior of the investigated materials can be taken into account. Besides, the strains occurring in the specimen geometries should preferably be complex, so that the validation does not investigate specific, narrow strain or stress states, but can also focus on the interpolation between calibration points of the used models. With regard to yield locus validation using the associated flow rule, this means that complex strain distributions form the basis for an effective investigation of interpolated curvatures in the yield function. In addition, complex strain distributions reduce the number of specimen geometries required, since the region of interest in the stress and strain space between uniaxial (UT) and equibiaxial tension (BT) is covered with just a few specimens. In combination with a test procedure that is as simple as possible, this results in a high efficiency of the validation. Finally, it is of great advantage to use a test that is not dominated by friction and where the friction effects can be separated from the influences of the material model parameters. This avoids the use of a friction model that is difficult to calibrate and prone to errors. Thereby, the results are dominated by material behavior, which is a key requirement for a validation of material models. The following bullets summarize the mentioned requirements for a validation test:

- Continuous collection of data over time
- Simple test procedure
- Small number of tests necessary
- Low friction influence
- Complex strain distributions from uniaxial (UT) to equibiaxial tension (BT)

State of the Art

A review of the state of the art shows that different tests are currently used for the validation of material models. These strategies for validation are mentioned in the following and evaluated with respect to the previously listed requirements for validation tests.

Standard *Nakajima experiments* are often used for evaluating predictive accuracy of material models [5–7]. Despite the presence of tool contact and thus friction, these experiments have the advantage that the results are not dominated by friction due to a suitable lubrication concept. As a result, no complex and error-prone friction model is required in the numerical representation of the experiment. Consequently, the quality of the material model can be directly assessed from the comparison between the numerical analysis and the experiments. Furthermore, when an optical measuring system is used, it is possible to measure strains on the upper side of the sheet quasi-time-continuously during the experiment. By means of numerical analysis of the test, the strain-dependent hardening behavior of the material can be compared with that of the material model. The central disadvantage of using the Nakajima experiments is that the strain distribution in the measuring area on the specimens remains within relatively narrow limits. To illustrate this, standard Nakajima tests were conducted using the material HC260Y [8] (1.0928 [9], similar to CR240IF [10]) with a sheet thickness of 1.0 mm. Figure 2 shows the strain

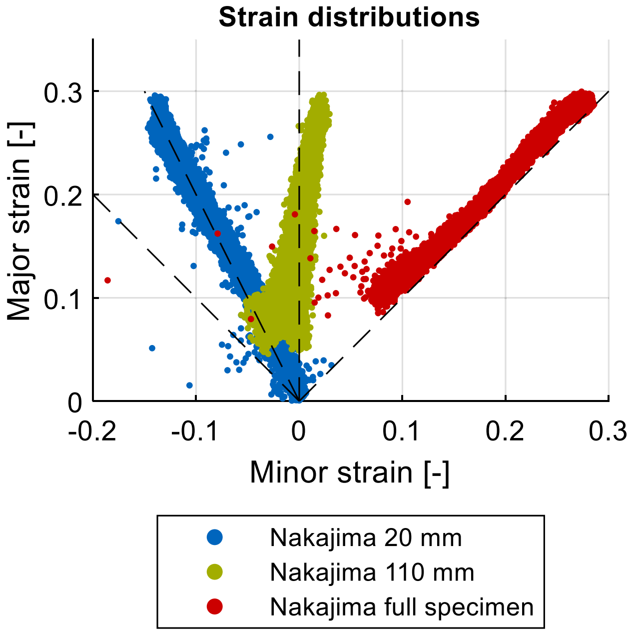

Fig. 2 Strain distributions of the entire observable specimen area for three different standard Nakajima specimens

distributions of the entire observable specimen area at a maximum major strain of about 0.3 for three different specimen geometries.

Significantly more complex strain distributions usually occur in industrial applications. Therefore, it must be ensured that these can also be reproduced with sufficient accuracy by means of numerical analysis. It is a great challenge for material models to numerically simulate complex strain distributions and the corresponding complex hardening behavior with sufficient accuracy. The Nakajima experiment is therefore suitable for evaluating and validating material models selectively for single stress states, but important factors of the models cannot be evaluated.

As further possibilities for the validation of yield loci, *tensile specimens of different geometries* are used [11–14]. Different stress and strain states can be realized with these specimen geometries. For example, tensile specimens with approximate plane strain states are widely used. The advantage is that in this case strains can also be recorded quasi-time-continuously by means of optical measuring systems. In addition, there is no tool contact in the area of strain measurement for tensile specimens, so that these tests are frictionless. These advantages allow direct validation of material models including their hardening behavior. The central disadvantage of using tensile specimens for the validation of material models is that the strain distribution remains within relatively narrow limits, which means that comprehensive validation is not possible.

In order to minimize this disadvantage, *tensile specimens with comparatively heterogeneous strain distributions* have been developed [15–18]. By means of these specimen geometries, it is possible to cover the strain range between pure shear and plane strain. However, due to the uniaxial load, it is not possible to represent the range between plane strain and equibiaxial strain with such specimen geometries. Furthermore, the specimen manufacturing in this case is comparatively costly due to the complex sample geometry.

All tests with strain distributions in comparatively narrow limits have in common that a large number of tests are required to cover and validate the relevant range in the stress space between uniaxial and equibiaxial tension, which makes this approach costly and time-consuming. Furthermore, it is not possible due to the narrow strain distributions to investigate the hardening behavior under complex load conditions, which is where several stress states occur simultaneously.

Another common experiment for evaluating material models is the *cross die* [19, 20]. The central advantages of the cross die are that the test conditions are comparable to industrial applications and that the parts have much more complex strain distributions than in the case of the previously mentioned tests. This makes it possible to evaluate the material model over a wide range of stress and strain states simultaneously. Nevertheless, the cross die also has significant disadvantages: since the tool concept does not contain any draw beads, thus making a material draw-in possible, the test is strongly dominated by friction. It is difficult to ensure well-defined, reproducible friction conditions in the experiments. The friction effect must of course also be considered in the numerical analysis. As a consequence, the influence of the material model cannot be explicitly evaluated; it can be evaluated only in combination with friction. This leads to difficulties in evaluating the numerical analyses meaningfully. In addition, it is not possible with the common available optical measuring systems to capture strains continuously when using the cross die. Only the initial and final state between the experiment and the numerical analysis can be compared. Since the hardening behavior is generally path-dependent, important information is lost in this respect. Moreover, this lack of continuous information over time often means that many experiments have to be performed in trial and error mode in order to achieve an adequate drawing depth that enables a meaningful comparison between the experiment and the numerical analysis.

Table 1 summarizes the currently used experiments for validating material models described in this chapter and assesses them with regard to the five identified requirements for validation experiments. The state of the art described shows that the area of validation tests for material models has much room for improvement. As a result, our motivation

Table 1 Current experiments for material model validation and assessment regarding predefinded requirements

Predefined requirements	Nakajima test	Simple strain tensile specimen	Complex strain tensile specimen	Cross die
Simple test procedure	✓	✓	✓	✗
Small number of tests	✗	✗	○	○
Low friction influence	○	✓	✓	✗
Complex strain distribution (UT…BT)	✗	✗	✗	✓
Continuous collection of data	✓	✓	✓	✗

was to invent a validation test that satisfactorily fulfils all of the predefined requirements for a validation test.

Used Material Models

Figure 1 illustrates that a wide variety of models exist for modeling material behavior, which differ in particular in their flexibility to represent real material behavior and the calibration complexity that usually correlates with this. In this work, the focus is on the basic elements of material models for sheet materials, the yield curve and the yield locus. More advanced models that represent damage and failure are not used or investigated here. Although this limits the possibility of validation up to the onset of material instability, this does not restrict the presented method for validating material models.

In the material models used, the yield curves are modeled in tabular form. The strain rate dependency of the materials is approximated using the m-value approach [21]:

$$\sigma_y = \sigma_{y0} \cdot \left(\frac{\dot{\varepsilon}^p_{\text{eq}}}{\dot{\varepsilon}^p_{\text{eq0}}} \right)^m \tag{1}$$

where σ_y is the Cauchy yield stress, σ_{y0} is the Cauchy reference yield stress, $\dot{\varepsilon}^p_{\text{eq}}$ is the equivalent plastic logarithmic strain rate, $\dot{\varepsilon}^p_{\text{eq0}}$ is the equivalent plastic logarithmic reference strain rate and m is the exponent for the strain rate dependency model.

In the context of this work, different yield locus models for plane stress with associated flow rule and isotropic yield locus hardening are used. The simplest model used is the first yield locus model of Hill (*Hill48*) [22]. In order to represent occurring anisotropy, the uniaxial anisotropy coefficients are used for calibration in addition to a yield curve. Alternatively, the *Hill48* model can be calibrated in stress space using the stress ratios (SR) under uniaxial and equibiaxial tension as calibration points (*Hill48 SR*) [23]. The yield locus models according to Barlat et al. (*Yld2000*) [24] and Banabic et al. (*BBC 2005*) [25, 26] allow the calibration of the uniaxial and equibiaxial stress states as well as the corresponding strain ratios. An exponent M defines the curvature of the interpolation between these calibration points.

The general form of the yield locus model with associated flow rule according to Vegter and van den Boogaard (*Vegter06*) is used as a basis for the following investigations [27]. Mathematically, the model is based on the interpolation of second-degree Bézier curves. The stress points under shear (FSH: $\sigma_1 = -\sigma_2$), uniaxial tension (FUN: $\sigma_2 = 0$), plane strain (FPS: $\dot{\varepsilon}_2 = 0$) and equibiaxial tension (FBI: $\sigma_1 = \sigma_2$) are used as reference points for the interpolation. The intersection points of the tangents at the stress points, called *hinge points*, give further control points for the interpolation. The tangents at the uniaxial tension points are determined using the uniaxial anisotropy coefficients (RUN). The tangent in the biaxial case is based on the equibiaxial anisotropy coefficient (RBI). The first principal stress for the stress point under plane strain is defined by the stress value FPS1, and the second principal stress is defined by ALPS, a value between 0 and 1 that defines the normalized location of the stress point of plane strain on the tangent between the adjacent hinge points. The tangent under shear is defined with a slope of 1. The assumption of tension–compression symmetry applies, so that only the region between shear and equibiaxial tension needs to be calibrated. Figure 3 shows the basic functionality of the *Vegter06* model with the reference and hinge points and the interpolation for one orientation with respect to the rolling direction in the principal stress system: [27]

The control points are determined for different orientations with respect to the rolling direction. Between these control points, Fourier series are used for interpolation. In this work, the control points are determined for angles of 0°, 45° and 90° regarding the rolling direction. In the equibiaxial load case, it is sufficient to define only one stress value (FBI) and one tangent (RBI0) for all rolling directions. Table 2 summarizes the 17 parameters which are necessary for the calibration of this model.

Uniaxial tensile tests are used as a basis for determining the flow curves and the parameters FUN and RUN, while hydraulic bulge tests are used to determine the equibiaxial parameter FBI. Both tests are standardized and can be classified as well-founded methods [28, 29]. The equibiaxial anisotropy coefficient was determined for one material based on the hydraulic test [30], for the other materials on the basis of the *Hill48* yield locus model according to

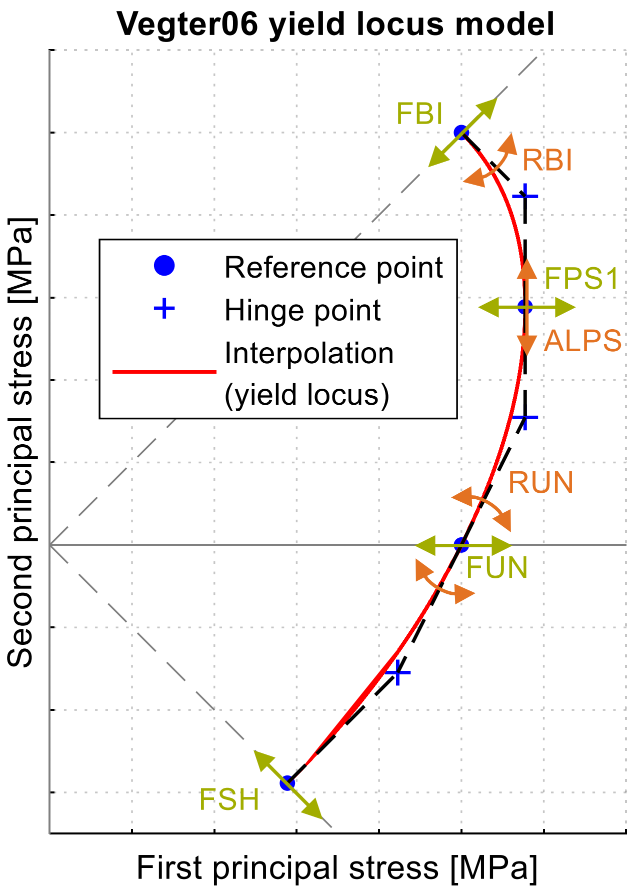

Fig. 3 Principle of the *Vegter06* model with the reference and hinge points and the interpolation (yield locus) for one orientation with regard to the rolling direction in the principal stress space. This model utilizes the associated flow rule. The arrows indicate the influence of the parameters on the yield locus

Table 2 Parameters for the *Vegter06* model using three rolling directions for the calibration

Parameter	Rolling direction		
	0°	45°	90°
FSH	FSH0	FSH45	FSH90
FUN	FUN0	FUN45	FUN90
RUN	RUN0	RUN45	RUN90
FPS1	FPS10	FPS145	FPS190
ALPS	ALPS0	ALPS45	ALPS90
FBI	=	FBI	=
RBI	RBI0	-	-

Eq. (2). This method of parameter determination may not provide the best possible representation of reality. Nevertheless, these methods are much less time consuming and demanding than is the use of inverse analysis [31] or the layer compression test [32]. In addition, this work focuses on the method of validation of material models, which allows the use of these identification methods.

$$\mathrm{RBI0} = \frac{\mathrm{RUN0}}{\mathrm{RUN90}} \tag{2}$$

The remaining parameters FSH, FPS1 and ALPS are derived from the *Yld2000* or *BBC* yield locus models. For this purpose, the exponent of the yield locus description M is defined, which, in combination with the aforementioned parameters, completely defines the *Yld2000* and *BBC* models. The stress points for plane strain and shear resulting in these models are adopted for the *Vegter06* model. The advantage of this method is that time-consuming, non-standardized tests can be avoided. Especially in the area of plane strain, various proposals exist for the calibration of the yield locus. These tests usually require an inverse numerical analysis or a large experimental effort [12, 33]. However, for motivation and verification of the MUC-Test, it is sufficient to derive the missing parameters from less flexible models. Thus, the *Vegter06* model reproduces the material behavior with the same accuracy as the *Yld2000* or *BBC* model. Furthermore, the *Vegter06* model can be modified locally, which forms the basis for a comprehensive parameter investigation in the following.

Investigated Materials

In order to investigate the suitability of the MUC-Test for validating material models for sheet metals, three materials of different material classes are examined. In addition to a microalloyed steel, a dual-phase steel (DP steel) and an aluminum alloy are investigated. The flow curves at 0°, 45° and 90° to the rolling direction were determined on the basis of uniaxial tensile tests in accordance with the standard [28]. The flow curve at 0° to the rolling direction serves as a reference flow curve ($\mathrm{FUN0} = 1$). The stress ratios of the flow curves of different rolling directions (FUN45, FUN90) were determined in the range of $8 - 12\%$ equivalent total engineering strain. The uniaxial anisotropy coefficients (RUN0, RUN45, RUN90) were determined according to [34] in the same strain range. The equibiaxial yield curve was determined by hydraulic bulge tests according to [29]. The equibiaxial stress ratio (FBI) was also averaged in the range of $8 - 12\%$ equivalent total engineering strain. In addition, the equibiaxial yield curve was used to extrapolate the uniaxial reference yield curve as described in [29]. Further *Vegter06* model parameters were derived from other models, as explained above. The data was analyzed with the aid of the MaterialModeler [35].

The primary focus of this paper is to present a methodology for the validation of existing material models. Consequently, the primary goal is not to use or determine the best possible material model for the materials under investigation. On the contrary, standardized and established basic methods and literature values were used to determine the material model parameters. Consequently, the use of very complex material models, for example with non-associated flow rule, was also avoided. In addition, the methods used for model parameter development do not correspond throughout. This may have an influence on the quality of the material models, but not on the presented methodology for the validation of material models.

Microalloyed Steel HC340LA

The first experiments were carried out with HC340LA [8] (1.0548 [9], similar to CR300LA [10]), a microalloyed steel with high yield strength with a sheet thickness of 1.0 mm. The elastic modulus was defined as $E = 210$ GPa and the Poisson's ratio as $\nu = 0.3$. Figure 10 includes the extrapolated reference flow curve at 0° to the rolling direction. The occurring yield point elongation is taken into account in the modeling. The strain rate dependency is modeled according Eq. (1) with a m-value of $m = 0.0048$ for an equivalent plastic logarithmic reference strain rate of $\dot{\varepsilon}^{p}_{\mathrm{eq0}} = 0.00025\ \mathrm{s}^{-1}$. The parameter values for the *Vegter06* model are summarized in Table 3. The stress values under plane strain and shear were determined based on the *BBC* model with an exponent of $M = 6$, the standard value for steel materials [36]. The resulting yield loci are shown in Figs. 4 and 5.

Dual-phase Steel DP590HD

Another material used was the high-ductility dual-phase steel CR330Y590T-DH [10] (DP590HD) with a sheet thickness of 1.0 mm. Elasticity was modeled with a Young's modulus of $E = 210$ GPa and a Poisson's ratio of $\nu = 0.3$. In Fig. 10, the extrapolated reference yield curve at 0° to the rolling direction is shown. The m-value of the strain rate dependency according Eq. (1) is $m = 0.0052$ for an equivalent plastic logarithmic reference strain rate of $\dot{\varepsilon}^{p}_{\mathrm{eq0}} = 0.00040\ \mathrm{s}^{-1}$. The parameter values for the *Vegter06* model are summarized in Table 4. The value for RBI0 in this case was determined in the hydraulic bulge test. The

Table 3 Parameters for modeling the yield locus of HC340LA using the *Vegter06* model

Parameter	Rolling direction		
	0°	45°	90°
FSH	0.5843	0.5489	0.5843
FUN	1	0.9780	1.0255
RUN	0.6680	1.0620	0.9040
FPS1	1.1190	1.1368	1.1667
ALPS	0.6743	0.6613	0.6090
FBI	=	1.0506	=
RBI	0.7389	-	-

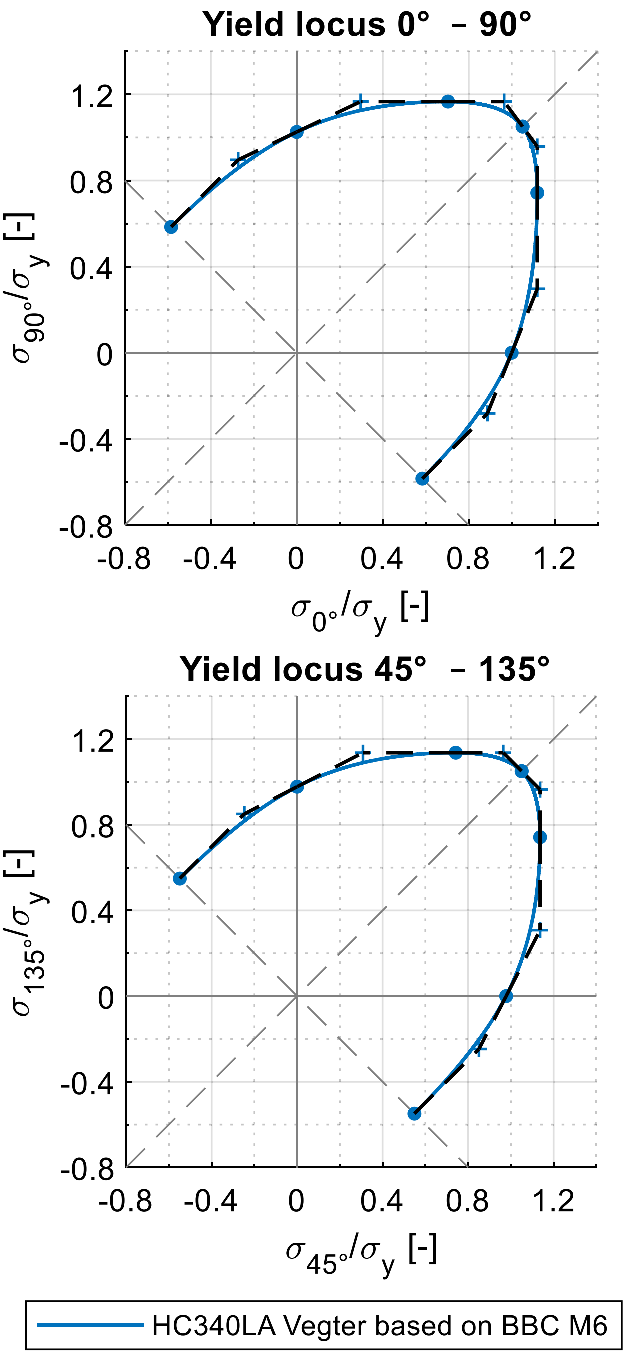

Fig. 4 Yield locus for the material HC340LA including reference and hinge points for the calibrated orientations

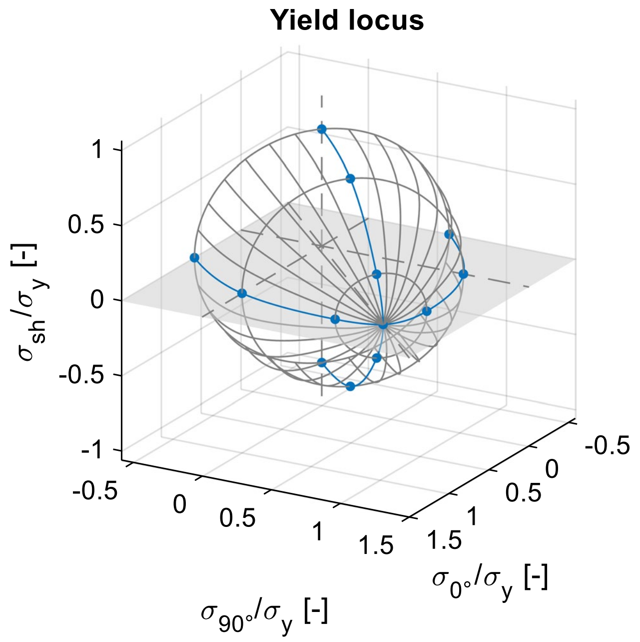

Fig. 5 Yield locus for the material HC340LA in 3D-representation. Calibrated orientations are colored

Table 4 Parameters for modeling the yield locus of DP590HD using the *Vegter06* model

Parameter	Rolling direction		
	0°	45°	90°
FSH	0.5595	0.5753	0.5595
FUN	1	1.0177	1.0132
RUN	0.9458	0.8630	1.2003
FPS1	1.1202	1.1247	1.1384
ALPS	0.5412	0.4977	0.4450
FBI	=	1.008	=
RBI	0.9854	-	-

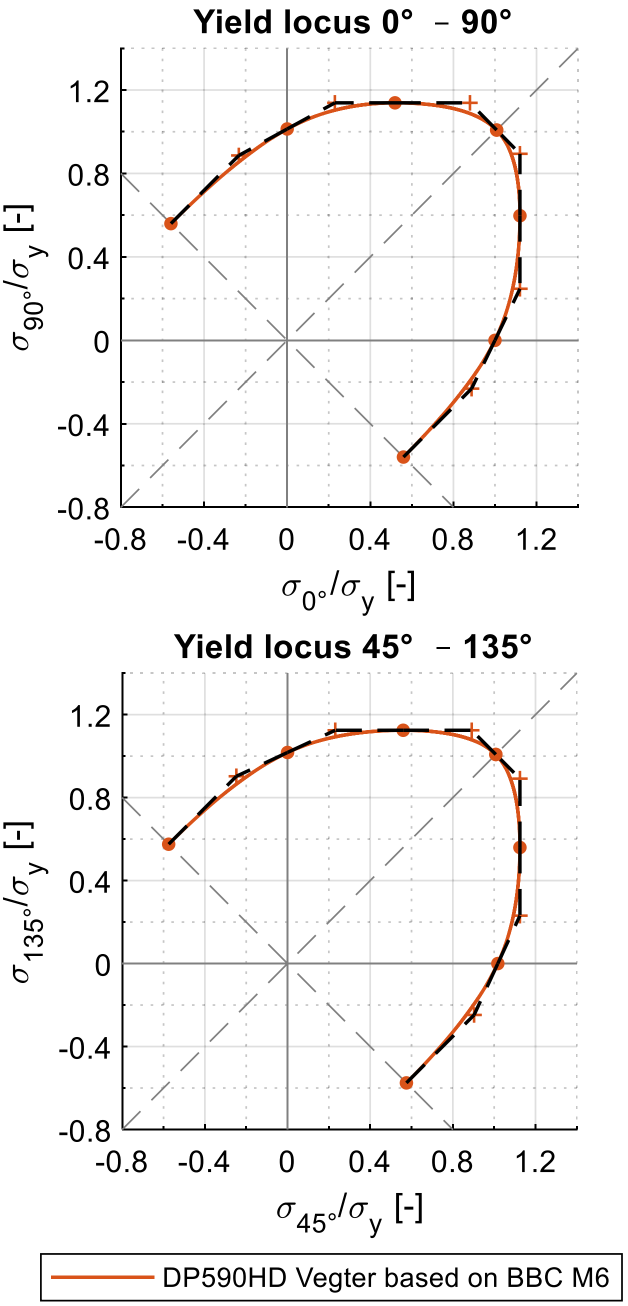

Fig. 6 Yield locus for the material DP590HD including reference and hinge points for the calibrated orientations

stress values under plane strain and shear were determined based on the *BBC* model with an exponent of $M = 6$ [36]. The resulting yield loci are shown in Figs. 6 and 7.

Aluminum AA5754

As a representative of an aluminum material, the naturally hard aluminum sheet AA5754 [37] (3.3535 [38] / A95754 [39] / AlMg3 [40]) with a sheet thickness of 1.0 mm was investigated. The elastic part of the deformation was modeled by Hooke's law with a Young's modulus of $E = 70$ GPa and a Poisson's ratio of $\nu = 0.33$. In Fig. 10, the extrapolated reference yield curve at 0° to the rolling direction is included. The aluminum material shows a negative strain rate dependency, which is represented by a m-value of $m = -0.0078$ and an equivalent plastic logarithmic reference strain rate of $\dot{\varepsilon}^{p}_{\mathrm{eq0}} = 0.00098\ \mathrm{s}^{-1}$ according Eq. (1). The parameter values for the *Vegter06* model are summarized in Table 5. Stress values under plane strain and shear were determined based on the *BBC* model with an exponent of $M = 8$, the standard value for aluminum materials [36].

The resulting yield loci in the calibrated stress planes 0° – 90° to the rolling direction and 45° – 135° are

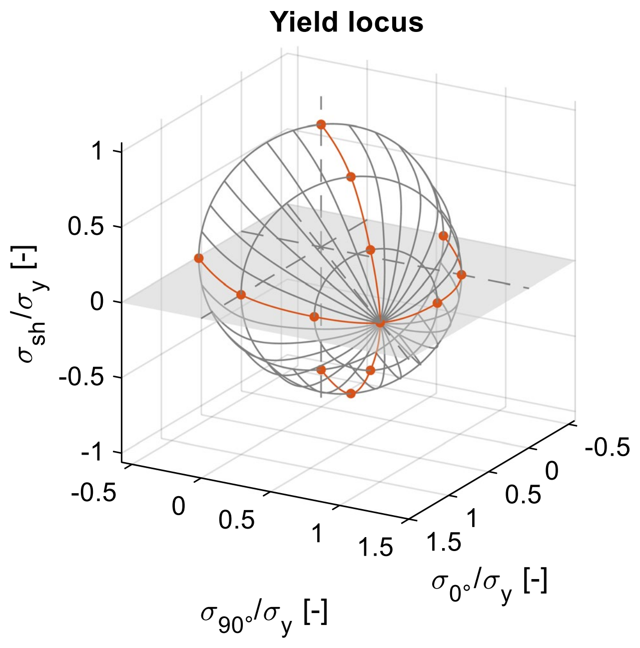

Fig. 7 Yield locus for the material DP590HD in 3D-representation. Calibrated orientations are colored

Table 5 Parameters for modeling the yield locus of AA5754 using the *Vegter06* model

Parameter	Rolling direction		
	0°	45°	90°
FSH	0.5523	0.5570	0.5523
FUN	1	0.9815	0.9771
RUN	0.7360	0.5953	0.6647
FPS1	1.0683	1.0514	1.0502
ALPS	0.4878	0.6447	0.6059
FBI	=	0.9757	=
RBI	1.1072	-	-

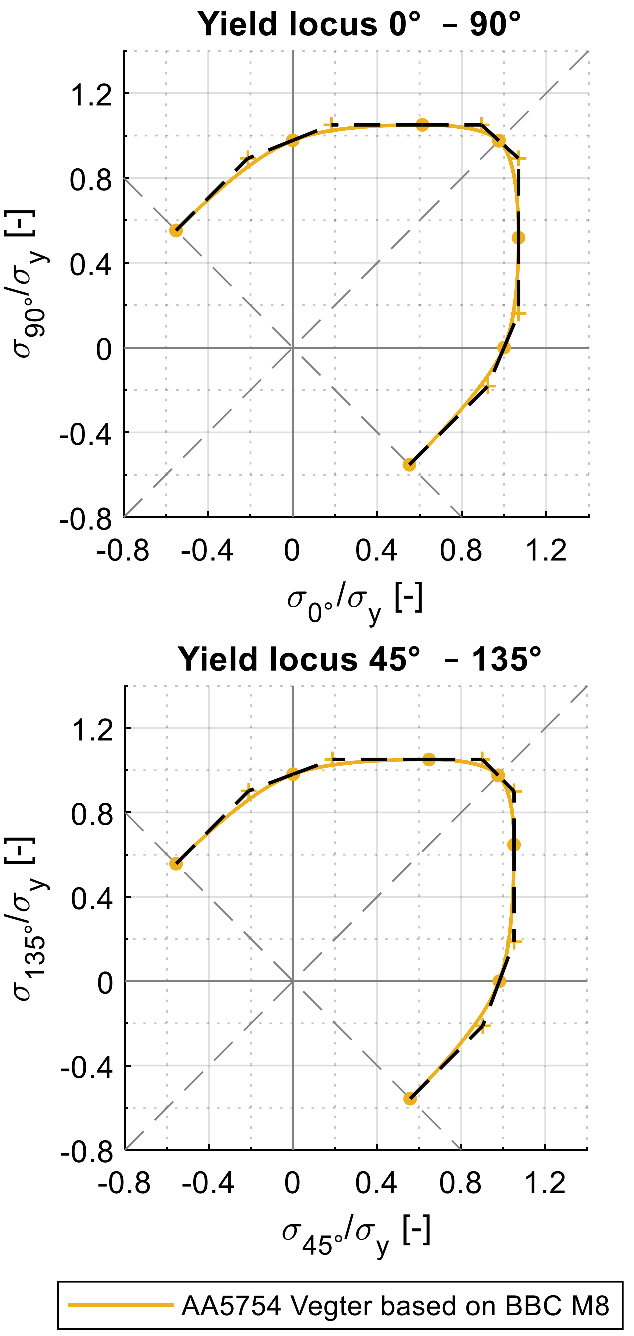

Fig. 8 Yield locus for the material AA5754 including reference and hinge points for the calibrated orientations

shown in Fig. 8. The interpolation between the calibrated planes resulting from the Fourier series is shown in the three-dimensional representation in Fig. 9.

Comparison of the Materials

The following figures show the flow curves (Fig. 10) and yield loci (Fig. 11) of the investigated materials in comparison. It can be seen that these are materials with significantly different strength and yield loci with distinctly different characteristics. These materials thus provide a good basis for investigations with the MUC-Test.

The MUC-Test

Design of the Tool

The main components of the forming tool called MUC-Test and their development are described in this section. An iterative process of tool construction in CATIA and numerical design investigations in AutoForm were conducted. The geometries of the tool (see Fig. 14) and the

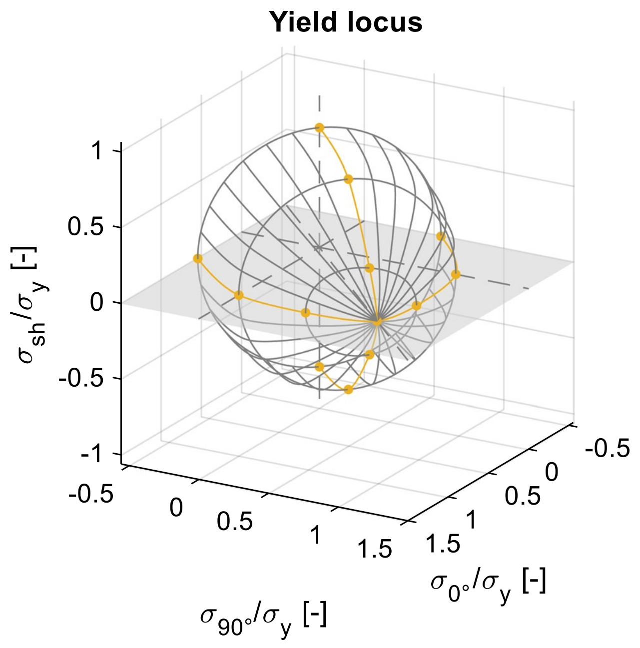

Fig. 9 Yield locus for the material AA5754 in 3D-representation. Calibrated orientations are colored

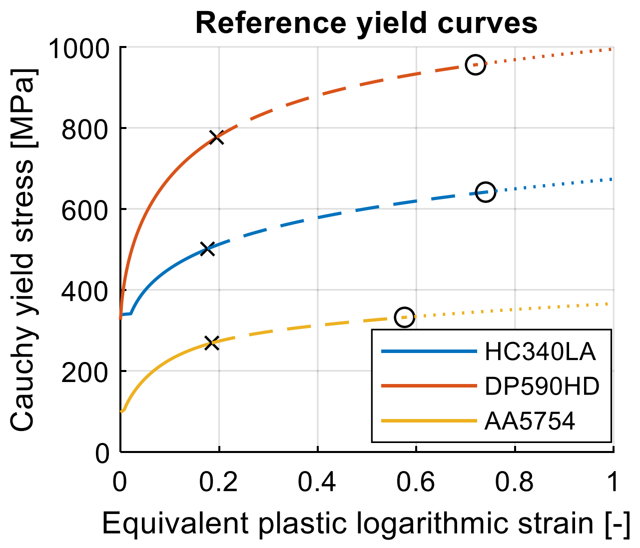

Fig. 10 Comparison of the yield curves of the investigated materials. The yield curves are based on tensile test data (solid line) up to the uniform elongation (black cross). The yield curves were extrapolated using hydraulic bulge test data (dashed line to black circle). The extrapolated range over the hydraulic bulge test data is shown as a dotted line

test specimens were manually modified and numerically examined and improved regarding the general requirements listed in the section General requirements for a validation test. For these preliminary numerical investigations, various standard material cards of different material classes (deep-drawing steel, dual-phase steel, aluminum) and different sheet thicknesses were examined.

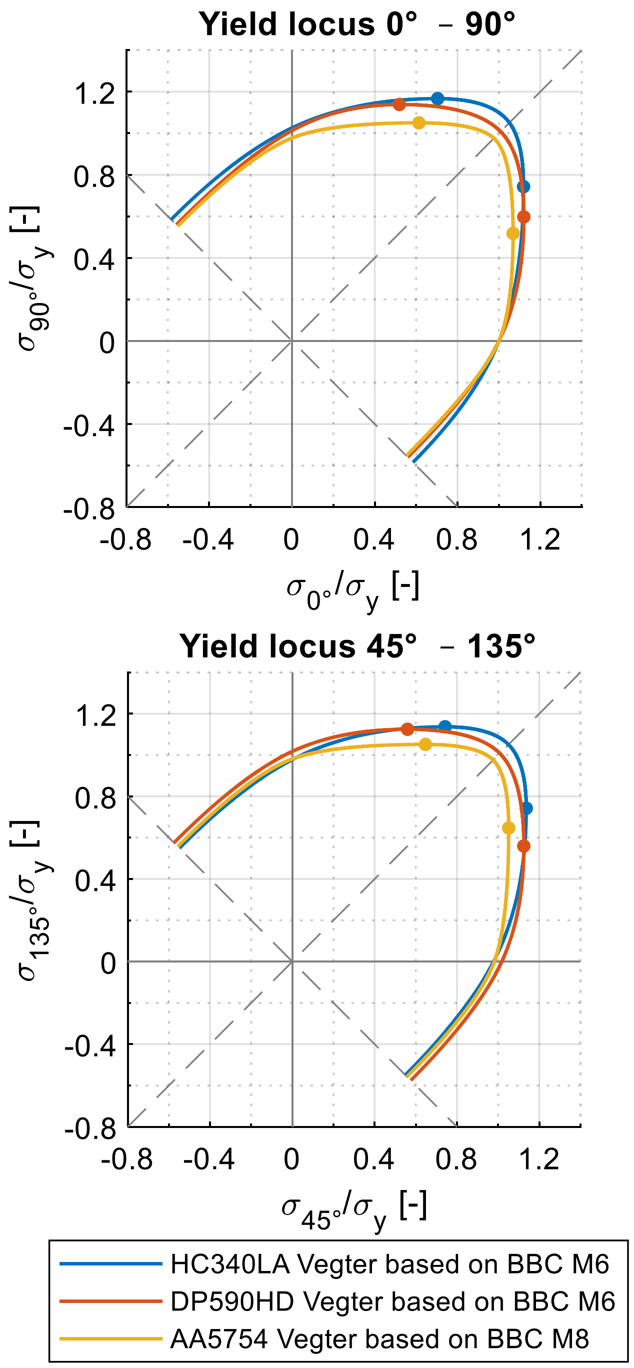

Fig. 11 Comparison of the yield loci of the investigated materials

The resulting tool geometry was subsequently manufactured. Figure 12 shows the three components of the tool: the punch, the blankholder, and the die.

The Nakajima test is widespread and is defined in the ISO 12004–2 standard [42]. Therefore, the size, the tolerances, and the mounting points of the new validation tool

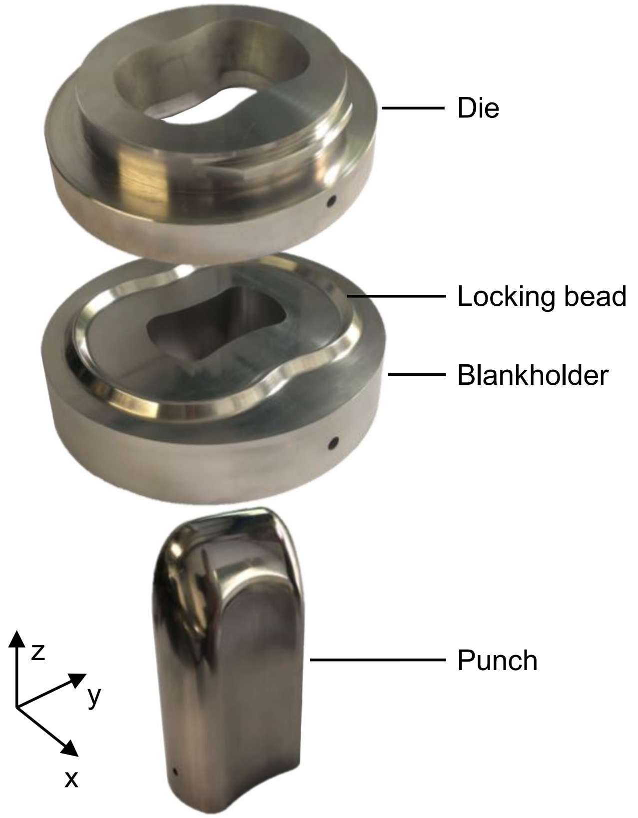

Fig. 12 The MUC-Test tool consisting of die, blankholder and punch (according [41])

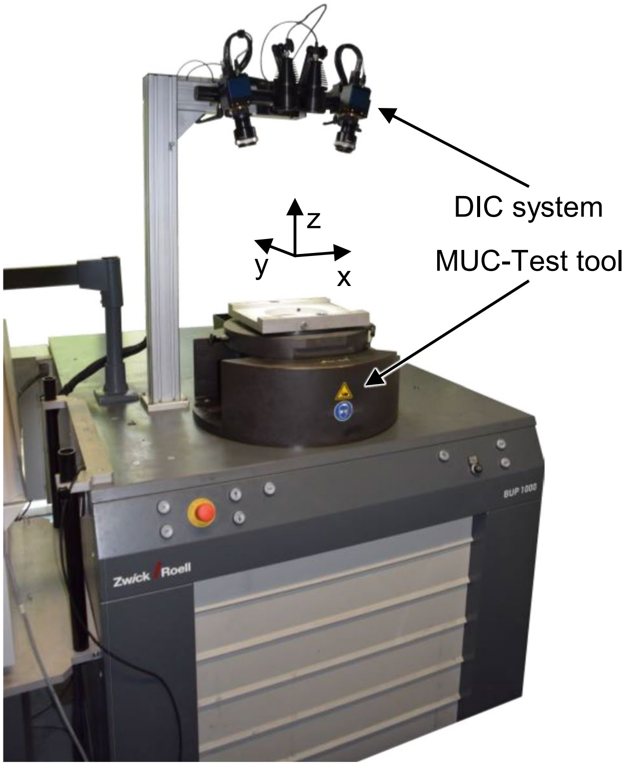

Fig. 13 Sheet metal testing machine used for the MUC-Test

are designed for a sheet metal testing machine also used in the Nakajima experiment: a BUP1000 from Zwick-Roell, shown in Fig. 13. This design guarantees a simple tool change with a short setup time. A piezoelectric load cell below the punch allows the measurement of punch forces.

One important requirement for the validation test is that the *test be easy to conduct*. It was therefore our aim to use only rectangular specimens able to be produced without a complex manufacturing process. The first numerical and experimental studies showed that it is possible to cover most of the strain space between uniaxial and equibiaxial tension with three sample geometries. This approach fulfills the requirement of a *small number of tests*. A specimen width of 70 mm was predicted for the region between uniaxial tension and plane strain. The area between plane strain and eqibiaxial tension is covered by a specimen with a width of 230 mm. This specimen is comparable to the biaxial test specimen in the Nakajima test and is also referred as *full specimen*. An additional sample with a width of 110 mm was used in the range around the plane strain. In the area of plane strain, the yield locus has a maximum. This sample geometry is therefore of central importance. The geometry of the punch influences the strain distribution significantly. The geometry description uses freeform surfaces mainly. Figure 14 shows the most important design features of this geometry description.

To achieve strain states in the region of uniaxial tension, a smooth radius of $r_2 \approx 378$ mm on top of the tool was chosen in the direction of the y-axis. The length of the arc (almost 50 mm) was chosen to be quite high in relation to the whole tool width of $w_y \approx 95$ mm. This enabled the 70 mm specimen to be stretched equally above the center of the punch. In addition, the smooth radius ensured that the material would flow from the outside to the inside in the y-direction. This allows negative minor strains which result in strains around the uniaxial tension region.

The radius decreases $\left(r_1 \approx 25 \text{ mm}\right)$ towards the edges in y-direction. Given the higher resistance against the movements of the blank, the smaller radius ensures expansion of the strain distribution towards the plane strain state. Consequently, the strain field moves towards the biaxial strain state with increasing specimen widths. Biaxial tension can be produced by the punch also having a radius $r_3 \approx 25$ mm in the x-direction. As a result, a uniform curvature exists at the outer ends of the punch geometry, and major and minor strains can increase to the same extent as with the full specimen.

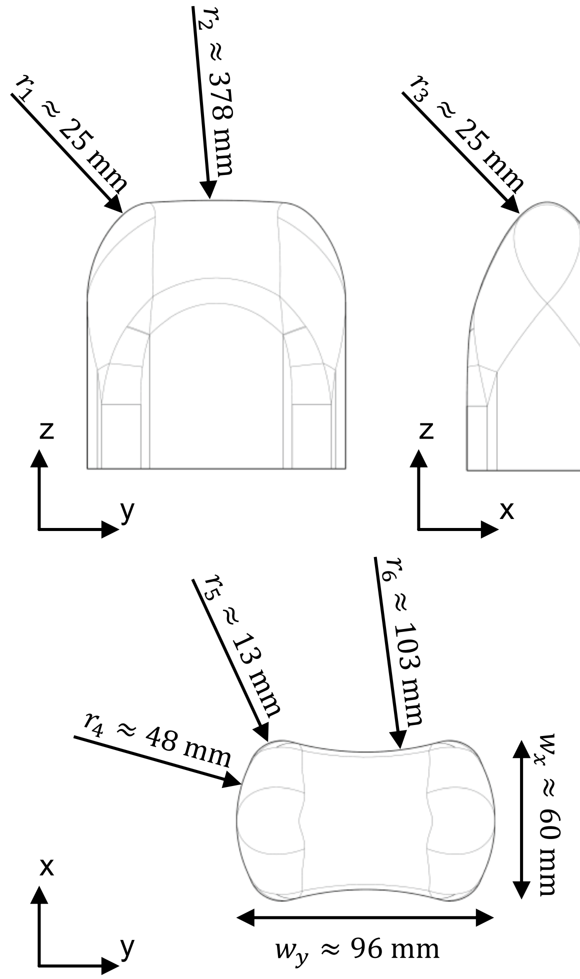

Fig. 14 Important design features of the punch

The die opening and the punch have an equivalent shape in the *xy*-plane, which resembles a butterfly. The minimum gap between punch and die is 5 mm all around. This butterfly shape increases the expansion of the strain distribution. The concave radii at the outer edges $\left(r_4, r_5\right)$ reduce the material flow. This shape reinforces the tendency of the material to stretch in a biaxial direction on the outer corners of the punch. In addition, the convex radius in the middle of the punch and the die $\left(r_6\right)$ enables high strains in the pole of the punch.

The strains of the sheet can be detected through the opening of the die using an optical measuring system. The ARAMIS 4 M digital image correlation (DIC) system from GOM was used in this case. The requirement of *continuous collection of data over time* could thus be fulfilled.

The last requirement is the *low influence of friction.* This can be fulfilled with a locking bead that is adapted to the butterfly geometry of the die. The height of the locking bead allows the testing of materials with a sheet thickness up to 1.5 mm.

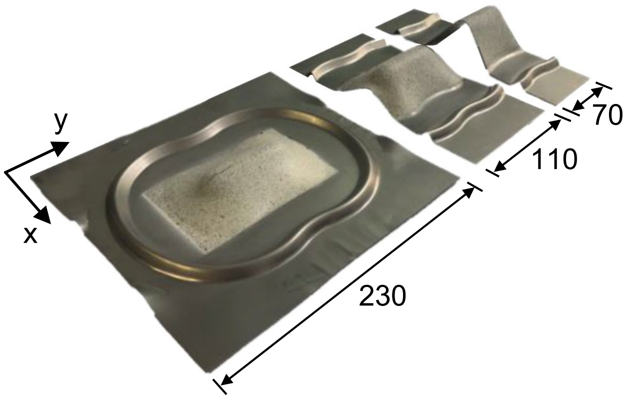

Fig. 15 Test geometries used at different widths: 70 mm, 110 mm and 230 mm (full specimen)

The established geometry seems to fulfill all requirements defined in the section General requirements for a validation test. The suitability of the MUC-Test for material card validation is investigated in the following subchapter in detail.

The geometric data of the tool is provided in the attachment of this publication.

Test Conditions

The experiments were conducted on a BUP1000 sheet metal testing machine (Fig. 13). The blankholder force used was 400 kN, and the punch speed was set to 1.0 mm/s. The lubrication system consisted of two layers of deep drawing foil and lubrication paste for the punch. No lubrication was used for the contacts between the specimen and the blankholder and the specimen and the die. The test was performed with three different widths of sample geometries, which are shown in Fig. 15: 70 mm, 110 mm and 230 mm (full specimen). The coordinate system of the specimen geometries is aligned to the coordinate system of the tool by means of distance measurement with a minimum accuracy of about ± 1 mm.

The specific orientation of the specimens relative to the rolling direction allows any area of the yield locus to be examined. The experiments were carried out in three different sample orientations in order to investigate this in detail. The angle between rolling direction and the *x*-axis (cf. Figure 15) describes the specimen orientation (0°, 45°, 90°). For the 3D strain measurement with the ARAMIS system, the specimens must be prepared with a stochastic spray pattern. The ARAMIS 4 M system has a camera resolution of 2400 pixels × 1728 pixels. The camera arrangement results in a calibrated measurement volume of approximately $x \times y \times z = 120\ \mathrm{mm} \times 85\ \mathrm{mm} \times 65\ \mathrm{mm}$. A facet size of

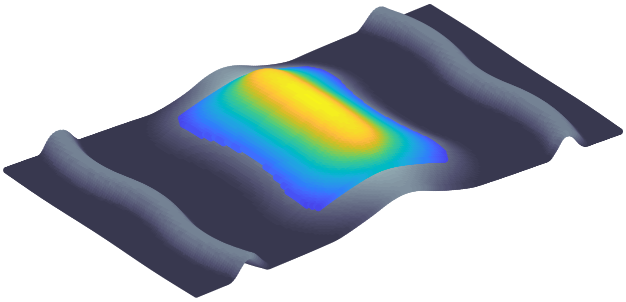

Fig. 16 By using a 110 mm specimen as an example, the area that is visible through the die opening for the DIC system is highlighted in color. For this area, the strains of the specimen's surface can be determined

19 pixels with a point distance of 16 pixels was selected for strain calculation. These settings result in a strain reference length (SRL) of about 1.45 mm. The strains occurring on the upper surface of the sheet are detected by the DIC system in the area of the die opening quasi-continuously over the whole punch stroke with a frequency of 10 Hz. The region for which the strains can be determined by means of the DIC system is shown in Fig. 16.

Processing of the Experimental Data

The data collected is on the one hand strains, determined by the DIC system, and on the other hand punch forces, measured by the BUP1000 machine. These two measuring systems are synchronized in time. The data is processed with a MATLAB tool. From the DIC data, the coordinates of the facet midpoints and the associated logarithmic strain tensors, including the principal strains in the sheet plane, are exported for each acquired step. Since the coordinate system of the DIC system generally does not match the coordinate system of the tool, the detected coordinates are aligned accordingly. As a result, the coordinate system of the experimental measurement results matches the coordinate system used in the numerical representation, and the data can be compared in the same coordinate system directly. Another quantity that needs to be determined for the DIC data is the time of the initial punch contact. This is realized by the averaged z coordinates in the visible region. If this value exceeds a defined limit, the punch is in first contact and the time of the previous stage is defined as the initial punch contact. A value of 0.02 mm for this limit has proven to be robust and sufficiently accurate. The punch force is exported from the machine data and the time stamps of the two measuring systems are synchronized.

Characteristics of Experimental Results

The first experiments were carried out with HC340LA, a microalloyed steel with a sheet thickness of 1.0 mm. Further material parameters can be found in the section Microalloyed steel HC340LA, where the numerical model is described in detail. For the material HC340LA, Fig. 17 shows the experimentally determined (Exp) principal strains for the three specimen geometries investigated with rolling direction in the x-axis (0°). The strain distributions are shown for a punch stroke at approximately 80% of the punch stroke with maximum punch force. This ensures that the strain distributions have already evolved sufficiently, but no strain localization occur yet and the forming process is still stable. In addition, the envelope of the strain distributions is

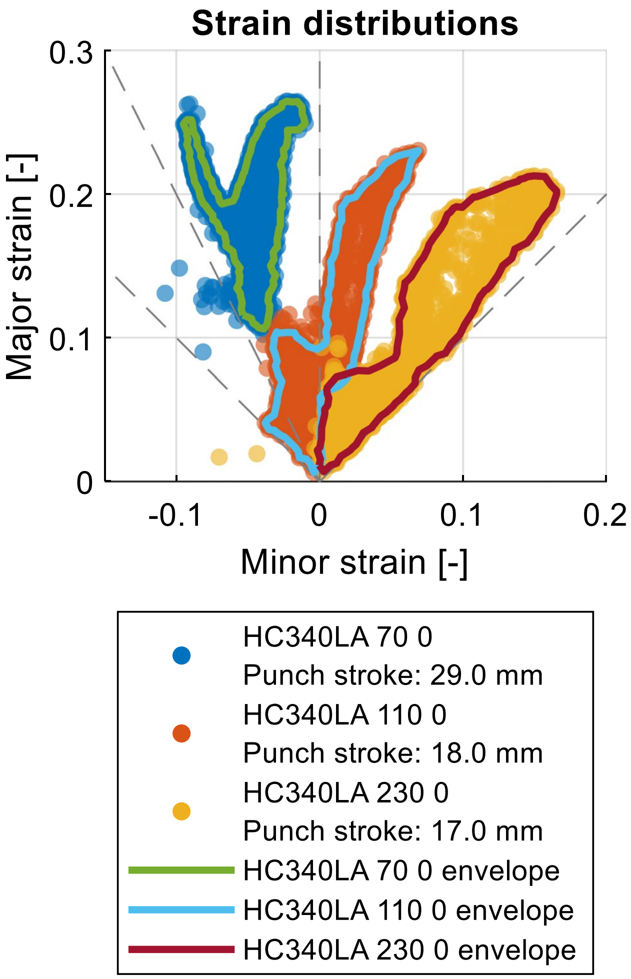

Fig. 17 Experimentally determined (Exp) principal strain distributions and their envelopes for the three specimen geometries investigated with rolling direction in the x-axis (0°) shown for a punch stroke at approximately 80% of the punch stroke with maximum punch force

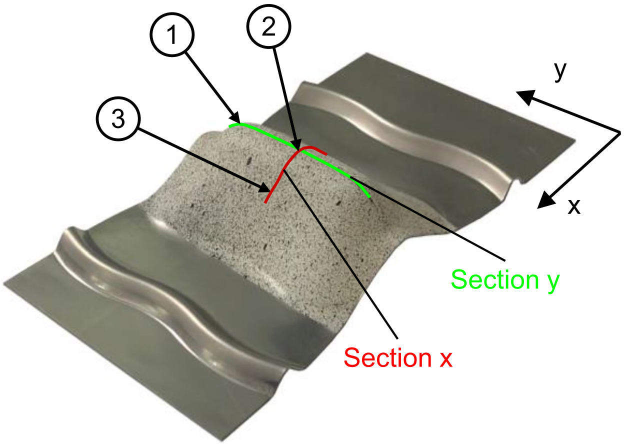

Fig. 18 Location of the sections and characteristic points on the specimen: (1) punch corner, (2) punch center, (3) flange

displayed, which is useful for comparing different strain distributions.

It is helpful to consider the strains along sections that contain characteristic geometry features of the punch in order to better understand the strain distribution characteristics that evolve. In Fig. 18, the two sections examined along the *x*-axis (section *x*) as well as the *y*-axis (section *y*) are shown in the visible region. In addition, characteristic points along the sections are marked: punch corner (1), punch center (2), flange (3).

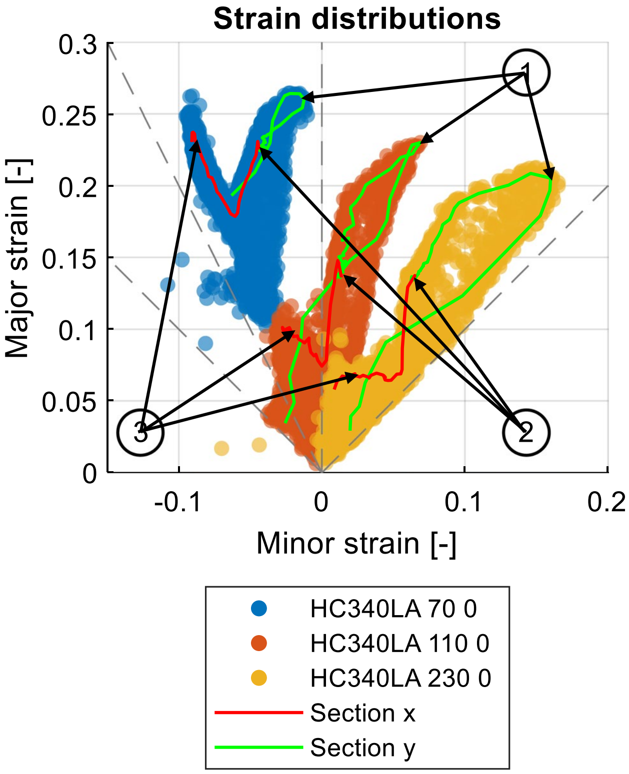

Fig. 19 Location of the sections and characteristic points in the strain distributions (Exp)

In Fig. 19, the strains along these sections and the location of the characteristic points in the strain distributions are marked. It is evident that the characteristics of the strain distributions are mainly defined by the areas of the punch corners (1) and the flanges (3).

The punch force is an integral measure of material strength over the entire specimen that can be measured easily. Hence, it is an additional parameter that can be fruitfully used for validation. Corresponding test results for the material HC340LA are shown in Fig. 20. The dashed lines show the punch strokes at which the strain distributions are plotted in Figs. 17 and 19.

Suitability for Material Card Validation

Besides the five general requirements for validation experiments presented in the chapter *General requirements for a validation test*, there are further basic requirements particular to the test results: An essential demand on test results is their *reproducibility*. The reproducibility of the MUC-Test has already been shown in preliminary studies [41]. In order to qualitatively examine the *influence of friction*, different lubrication concepts were investigated. Further, it must be possible to resolve and *represent differences in material properties* using the validation test. Experimentally, this was investigated by testing different specimen orientations

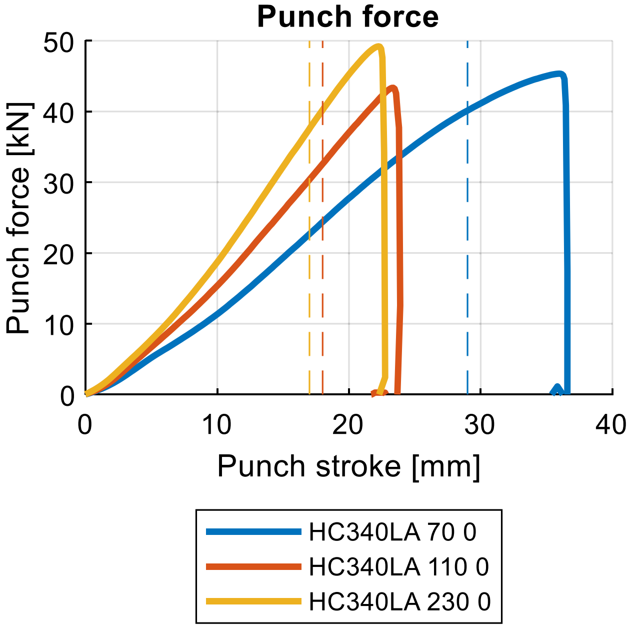

Fig. 20 Punch forces (Exp) for the three investigated specimen

regarding the rolling direction. By examining these points, it is possible to ensure that the MUC-Test is suitable as a basis for material card validation.

Experimental Studies on Punch Friction

The aim of the validation test is to ensure that the friction between the test sheet and the tool elements does not dominate the test. This can be investigated qualitatively on the one hand experimentally with different lubrication concepts for the punch (current chapter), and on the other hand by means of numerical investigations (chapter *Investigation of process parameters*). Figure 21 shows strain distributions for the standard lubrication concept for the punch consisting of two layers of deep-drawing foil and lubricating paste as well as with deep-drawing oil lubrication.

It can be seen that friction has a noticeable influence on the strain distributions of all three specimen geometries. However, it can be assumed that the friction between the punch and the sheet is significantly higher with oil lubrication compared to standard lubrication with two-layer deep-drawing foil and lubricating paste. Despite the apparent differences, the position, but not the characteristics of the strain distributions changes significantly. It can therefore be concluded that the test is not friction-dominated insofar as differences in material behavior result in different strain distributions. However, the investigation shows that friction cannot be disregarded in a numerical representation of the test and must be sufficiently modeled.

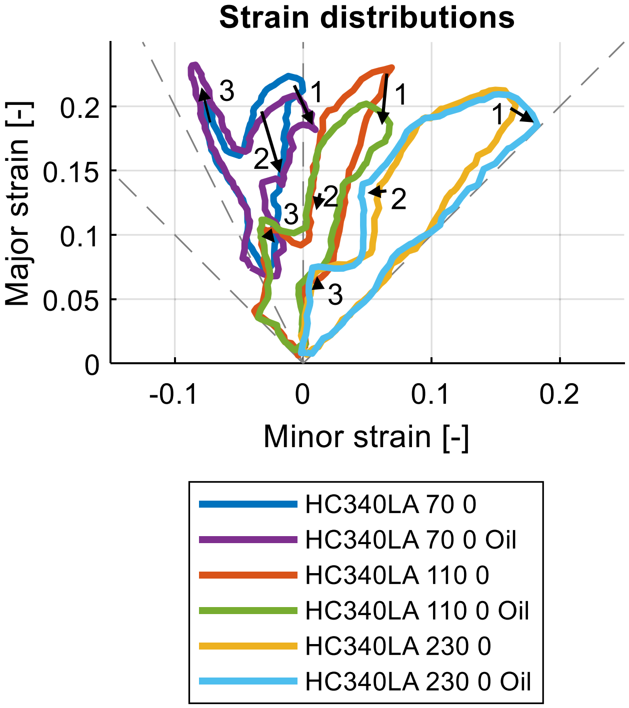

Fig. 21 Comparison of the strain distributions (Exp) for the standard lubrication concept as well as deep drawing oil lubrication for the punch. The arrows indicate the change of the characteristic points (1: punch corner, 2: punch center, 3: flange, cf. Figure 18) from the standard lubrication concept to oil lubrication

Influence of Different Material Properties

A key requirement of the validation test is that the resulting strain distributions depend significantly on the material properties. This is the case if the characteristics of the strains change accordingly with different material properties. To demonstrate this, the three specimen geometries used are investigated with orientations of 45° and 90° with respect to the rolling direction in addition to 0°. For non-isotropic materials, differences in the strain characteristics of the specimens can be expected for the different rolling directions. Figure 22 shows the comparison of the strain distribution envelopes. In particular, differences are evident in the strain distributions of the

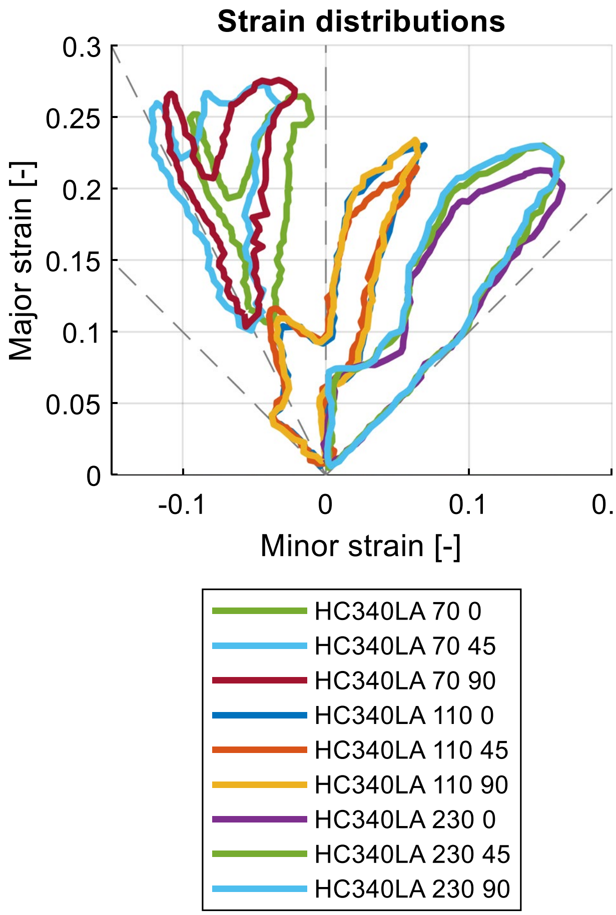

Fig. 22 Strain distributions (Exp) for the three specimens under varying orientation regarding the rolling direction

70 mm specimens. The strain distributions differ mainly by a clockwise rotation. This correlates with the anisotropy coefficients shown in Table 3 (RUN0 = 0.6680, RUN45 = 1.0620, RUN90 = 0.9040). This parameter represents the ratio of strain in the width to thickness direction for uniaxial tension. The larger the value, the more material flows from the width and the less from the thickness. For the uniaxial tension condition, the width strain is approximately equal to the minor strain. Thus, in comparison with the anisotropy parameters, the 45° specimen is expected to be the first specimen in the clockwise direction, then the 90° specimen, and then the 0° specimen, which corresponds to the representation in Fig. 22. Besides, the strain characteristic changes in the 45° specimen in such a way that a third branch appears in the envelope, which is due to strains on the punch center (characteristic point (2) in Fig. 18).

The differences in the strain distributions finally show that the MUC-Test is suitable as a basis for efficient and effective validation of material models for sheet materials. In addition to the predefined requirements (continuous collection of data over time, simple test procedure, small number of tests necessary, low friction influence, complex strain distribution), it could be shown that the test provides reproducible results [41] and that the strain characteristics vary for different material properties.

The Digital Twin of the MUC-Test

Setup of the Numerical Representation

Besides the experimental conduction of the validation tests, the digital twin of the test in the form of a FE simulation forms the second essential element of the validation strategy. For the simulation, the FEM tool LS-DYNA from Livermore Software Technology is used. In this chapter, important parameters of the numerical representation are pointed out. The verification and robustness of the simulation model are investigated in the chapter *Investigation of numerical parameters*. The simulation setup is shown in Fig. 23.

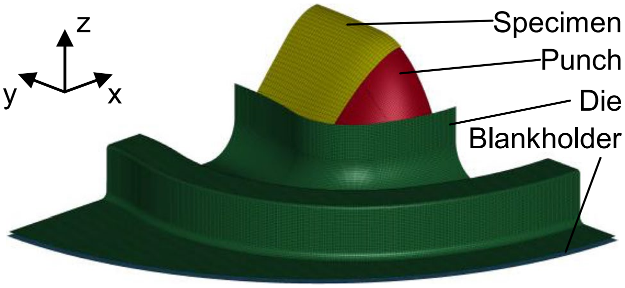

Fig. 23 Set up of the numerical representation of the MUC-Test in LS-DYNA

The geometry of the MUC-Test has a double symmetry with respect to the *x*- and *y*-axes. Accordingly, the setup is simulated as a quarter model, which significantly reduces the required computation time. Boundary conditions are activated at the symmetry planes, which prevent node movement orthogonal to the symmetry planes. The tool elements, consisting of die, blankholder and punch, are modeled as rigid bodies and meshed with four-node bilinear shell elements with an edge length of 0.5 mm. The specimen geometries are modeled using deformable, four-node bilinear shell elements with an edge length of 1.0 mm. The sheet thickness including its local change is taken into account in the numerical analysis. The fully integrated shell element (shell type 16) is used as the element type. Five integration points are calculated over the sheet thickness. Since in the experiments the strains are determined on the sheet surface, equivalent values must also be determined on the sheet surface in the simulation. Therefore, the Lobatto integration is used, since the outermost integration points are located on the sheet surface in this case. Due to the use of a quarter model, a quarter of the real applied blankholder force is applied compared to the test. By time scaling, the simulation time can be significantly reduced. In the numerical representation, the closing of the blankholder is simulated at a speed of 1000 mm/s, the punch stroke at a speed of 2500 mm/s. *Mass scaling* is not used in this simulation because the simulation results change significantly when it is used, as will be shown in the *Sensitivity analyses*. The material models listed in the chapter *Investigated materials* are used to describe the material behavior of the samples. For post-processing, the following quantities are exported from the simulation:

- Node coordinates and their connectivity
- Cauchy stress tensor
- Logarithmic strain tensor
- Punch force
- Punch stroke

Processing of the Numerical Data

The data exported from the simulation must be processed so that it can be used for further investigations. For this post-processing, a tool written in MATLAB is used. After the data is read in, it is trimmed to the area visible in the experiment. The actual local sheet thickness is calculated using the strains in the sheet thickness direction of the center integration point (sheet center plane). Since in the experiment the strains are detected on the upper side of the sheet, the corresponding data of the numerical representation have to be prepared. Consequently, the strains and stresses on the top side of the sheet are read out. For this purpose, the topmost integration point can be used, since it is located on the top side of the sheet due to the selected Lobatto integration. From the general strain tensor, the major/minor strains in the sheet plane are determined. For the comparison between experiment and simulation, the nodes have to be projected onto the top side of the sheet. For this purpose, the normal vectors are calculated from the node coordinates and their connectivity information for each element. For each node, the normals of the adjacent elements are averaged and the nodes are shifted along the resulting vector by half the sheet thickness towards the top of the sheet. A special case arises at the symmetry planes, since here a displacement orthogonal to the plane is not allowed. In order to allow uniform data handling, all quantities for each element are projected onto the nodes. Here, the isoparametric concept is used [43]. This results in four node values for each element. Due to the compatibility condition, displacements at the nodes are continuous. This is not necessarily the case for stresses and strains. Accordingly, representative stress and strain values can be determined for each node by averaging its nodal values of adjacent elements.

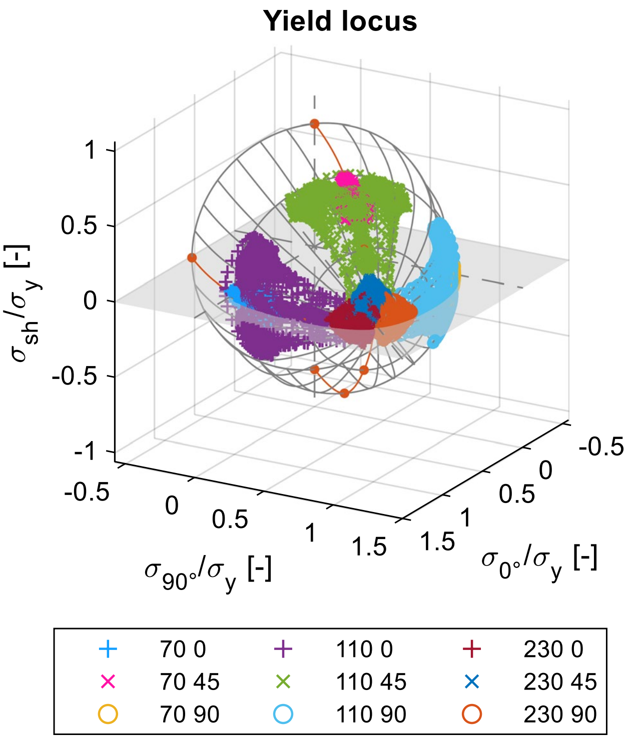

Fig. 24 Yield locus in 3D-representation (Fig. 7) and stress distributions for the three investigated specimens in three directions regarding the rolling direction exemplarily for the material DP590HD for a punch stroke at 80% of the punch stroke at maximum force

The prepared stress data can be plotted in the 3D representation of the yield loci. This makes it clear in which region of the yield locus the stresses are located for the punch stroke under consideration. In Fig. 24, the stress distributions of the studied specimen geometries are plotted for the three studied orientations with respect to the rolling direction for a punch stroke at 80% of the punch stroke at maximum force. The symmetries resulting from modeling as a quarter model were taken into account. It can be seen that by means of the three specimen geometries used and the three orientations investigated with respect to the rolling direction, it is possible to cover all the main zones of the yield locus over a large area. This allows validation of yield locus models not only for narrowly limited stress conditions, but also validation of the interpolation in the form of the curvature of the yield locus. This illustrates that the predefined requirement regarding complex strain distributions (section General requirements for a validation test), which also results in complex stress distributions, proves to be useful for an effective validation and that this requirement is fulfilled by the MUC-Test.

Data Comparison Approach

The basis of validation is the comparison between experiments and simulations. Furthermore, besides validation, it is of interest to investigate different parameters. The parameters of interest can be divided into numerical parameters, process parameters and material model parameters. Here, as a basis, a comparison of two simulations with different parameters is useful. This enables

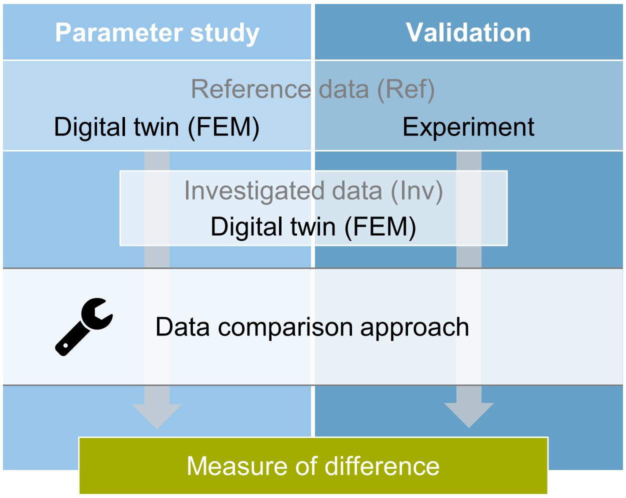

Fig. 25 Schematic flowchart of the data comparison approach for use in parameter studies and validations

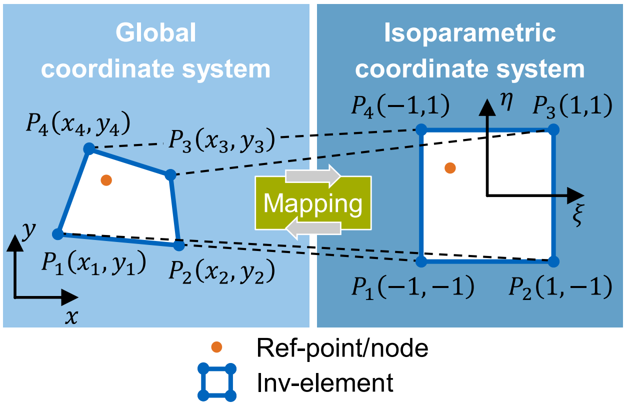

Fig. 26 Scheme of isoparametric mapping for a quadrilateral element (based on [44])

a systematic numerical analysis of different influencing factors, which would be easier to handle when comparing them with experiments. An essential goal of this work was therefore to create a tool which is able to compare

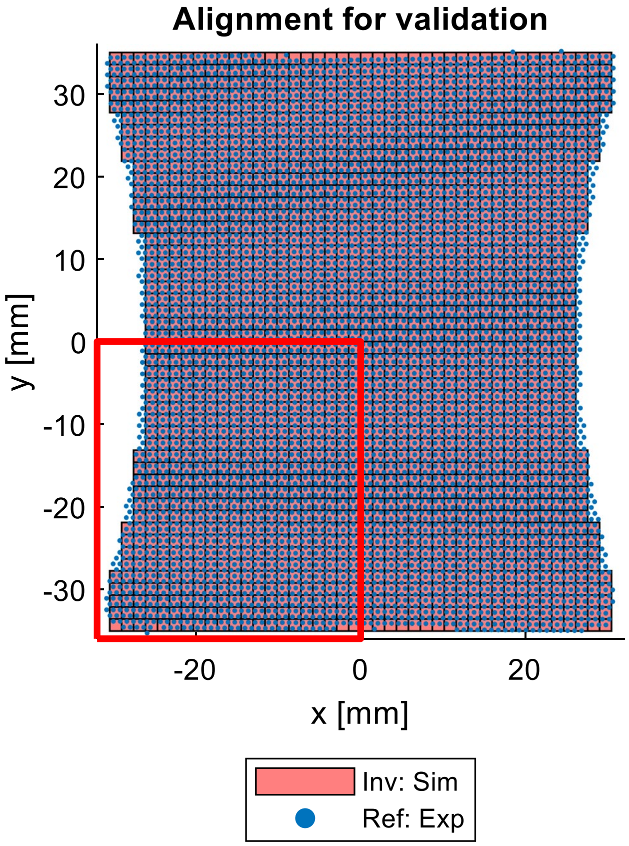

Fig. 27 Alignment of the coordinates in the visible region (see Fig. 16) for experiment (Exp) and numerical representation (Sim) as used for validation. For parameter studies (Ref: Sim, Inv: Sim), it is sufficient to compare the data of the quarter models (red bordered area)

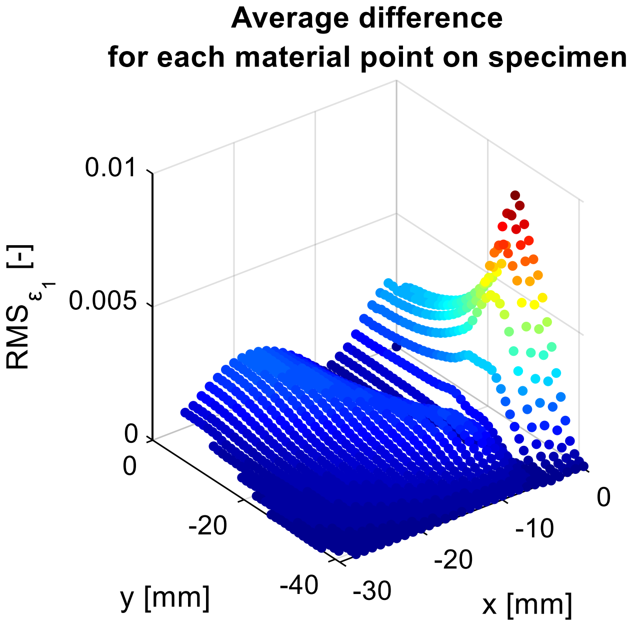

Fig. 28 Difference in major strain between two exemplary FE simulations weighted by equivalent strain and averaged for each material point in spatial resolution

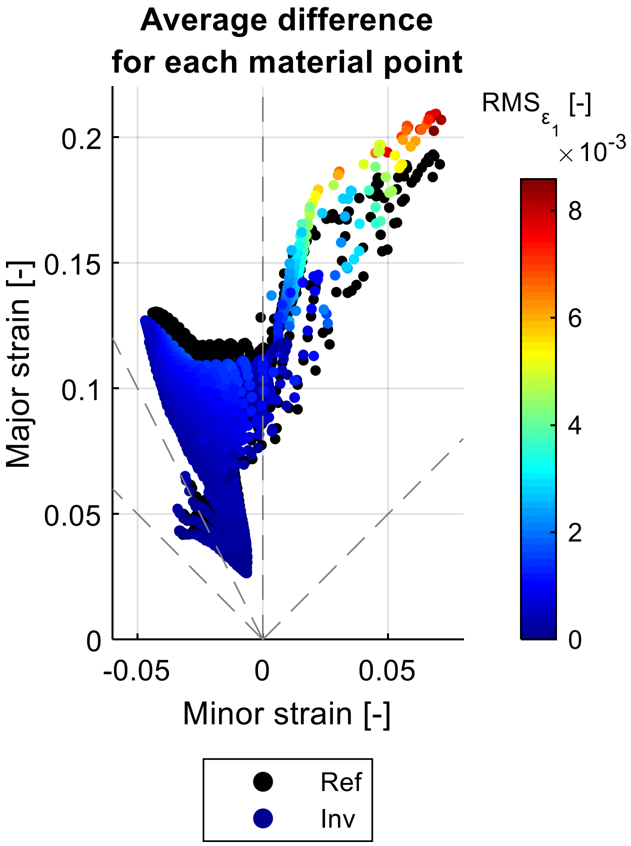

Fig. 29 Strain distributions for the two exemplarily investigated FE simulations. The color of the investigated data (Inv) represents the difference in major strain between the compared FE simulations weighted by equivalent strain, averaged for each material point

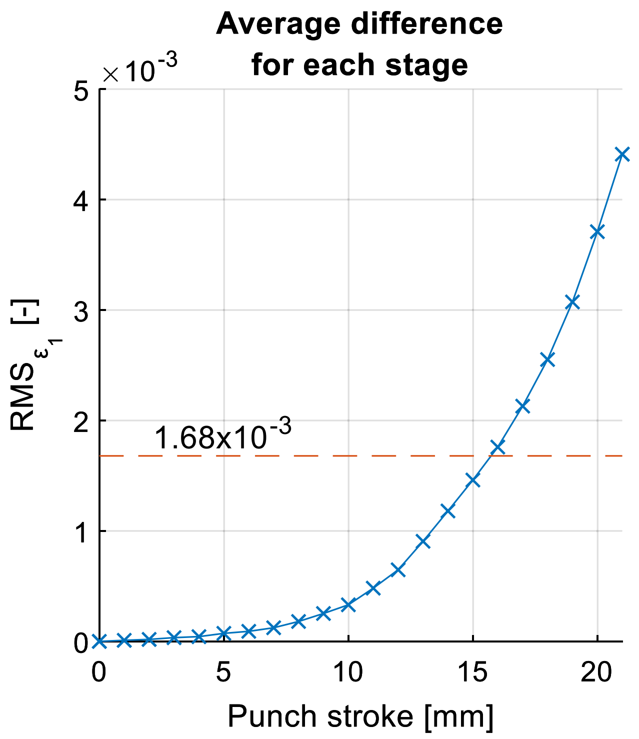

Fig. 30 Difference in major strain between the exemplarily compared FE simulations averaged for each investigated stage. The dashed line marks the total difference

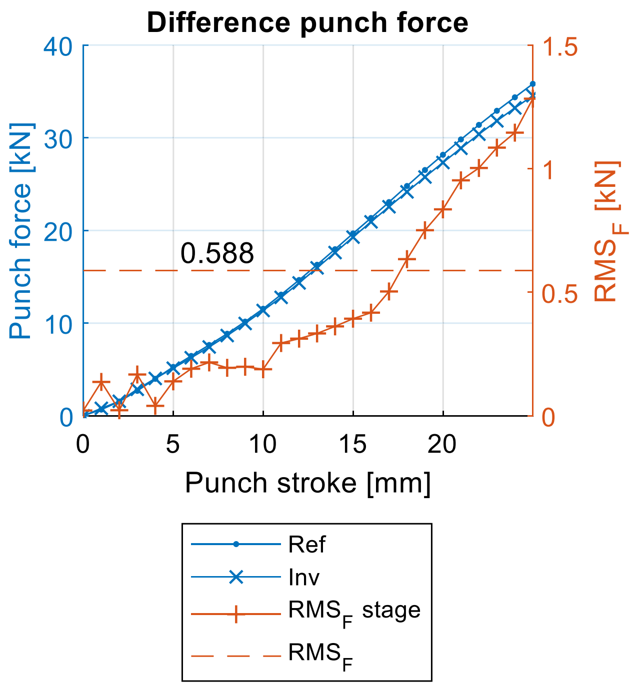

Fig. 31 Punch force versus punch stroke of the reference (Ref) and investigated (Inv) data (axis left). Difference between Ref and Inv versus punch stroke and total difference (axis right)

experiments with simulations as well as two simulations with each other in the same way and to determine a measure for their differences. This program provides the basis for parameter studies and finally the validation of material models. The data comparison approach is shown graphically in Fig. 25.

In this work, the principal strains in sheet plane for all detected intermediate states quasi-continuous over the punch stroke as well as the punch force serve as comparison quantities between the reference data (Ref) and the data under investigation (Inv). The punch force represents a scalar quantity over the punch stroke: $F(h)$. Thus, for a comparison of punch forces, a scalar comparison over the punch stroke is sufficient. The strains, in contrast, represent a spatially resolved strain for each determined stage: $\varepsilon_{1,2}(h,\boldsymbol{x})$. In order to use the entire information of the determined strain fields, a full-field comparison is realized for each determined state. The quantities are compared in the punch stroke range $h = 0 - 0.8 \cdot h\left(F_{\max}\right)$. In this punch stroke range, the forming process is stable. Material failure in the form of localizing strains does not yet occur. The focus in this work is on the basic elements of the material models, the yield curve and the yield locus. More advanced models for damage and failure prediction are not of primary interest here. Although this limits the possibility of validation up to the onset of material instability, this does not limit the presented method for validation of material models.

Full-field Comparison of Strains

A full-field comparison allows the entire strain information determined (see Fig. 16) between reference data (Ref) and investigated data (Inv) to be used to determine a difference. In this way, the comparison is based on the largest possible database. This avoids the possibility that something important to the investigation is not taken into account due to clipping of the data. However, this approach carries the risk that, when determining an overall difference between reference and investigated data, a large number of data of little relevance could make the method insensitive with respect to important differences. In order to allow the advantages of a full-field comparison with as meaningful results as possible, a weighting of the data is introduced in the calculation of the difference.

The essential requirement for a full-field comparison is that reference data (Ref) and investigation data (Inv) are compared at equivalent points. This is the case when the same material points are tracked and compared over the entire punch stroke. This is satisfied when the principal strains of the Inv-data are determined at the coordinates of the nodes or points of the Ref-data. Since

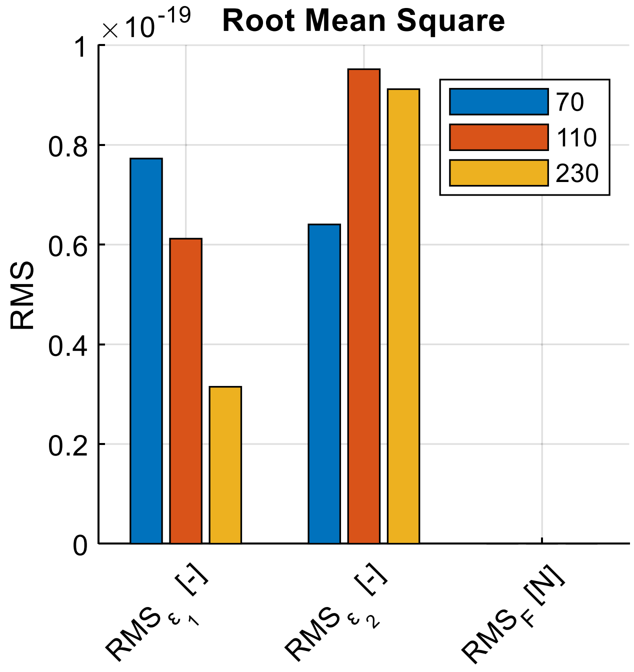

Fig. 32 Differences in major strain, minor strain and punch force for the three investigated specimens (70 mm, 110 mm, 230 mm) resulting from the data comparison approach for using the same data as reference and investigated data

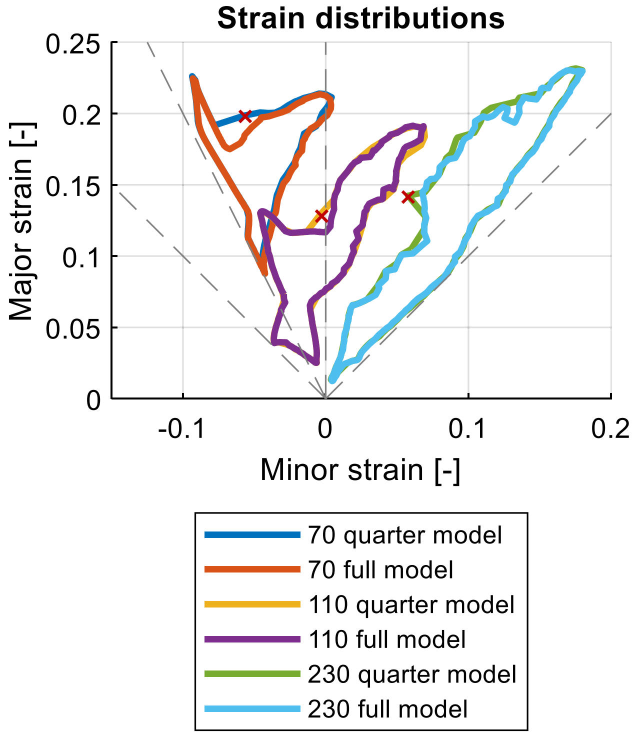

Fig. 33 Comparison between quarter model and full model by envelopes of the simulative determined (Sim) strain distributions. The points of most relevant difference are marked with a red cross

data from FE simulations is always used as Inv-data (cf. Figure 25), the isoparametric concept can be used here [43]. Schematically, the principle of isoparametric mapping is shown in Fig. 26.

Here a difference between a validation and a parameter study arises: since it must be assumed that the experiments are not completely symmetrical, the Inv-data is completed from a quarter model to a full model in the case of validation, see Fig. 27. In the parameter study, it is sufficient to compare the data of the quarter models (red bordered area in Fig. 27). The resulting difference must therefore be normalized to the number of examined Ref-nodes/points to allow comparability between parameter study and validation.

For the realization of the isoparametric concept, first for each element of the Inv-data the points/nodes are determined which lie within or on the edge of the element. The element and the nodes are now transferred into the isoparametric space and the location of each node is determined using the two parameters ξ and η. This uniquely defines the location of the Ref-node within the element. This determination of the isoparametric parameters needs to be performed only in reference configuration. The position of the material point within the element does not change over the forming process. Consequently, for a comparison of equal material points, the parameters ξ and η are constant over the entire punch stroke. Using these parameters and the shape functions of the elements used, the strains of the Inv-data can be interpolated at all nodal coordinates of the Ref-data for each calculated state. This results in a database that provides principal strains at equivalent coordinates over the entire punch stroke, which allows a difference between Ref- and Inv-data to be determined for each material point at each state. The values of the Ref-data at the determined states of the Inv-data is obtained by linear interpolation to quantify the difference in certain punch strokes. A modified form of root mean square (RMS) is used as the measure of difference in this work. In the following Eq. (3), i = 1 … k represents the control variable for the state or punch stroke, j = 1 … n the index for the nodes. k is the sum of all examined states, n the sum of examined nodes/points.

$$RMS_{\varepsilon_{1,2}} = \sqrt{\frac{\sum_{i,j=1}^{k,n}\left[\left({}^{i,j}\varepsilon_{1,2}^{Inv} - {}^{i,j}\varepsilon_{1,2}^{Ref}\right)\cdot\frac{{}^{i,j}\varepsilon_{eq}^{Inv}}{\max\left({}^{i}\varepsilon_{eq}^{Inv}\right)}\right]^2}{k\cdot n}} \tag{3}$$

The factor $\left[{}^{i,j}\varepsilon_{eq}^{Inv}/\max\left({}^{i}\varepsilon_{eq}^{Inv}\right)\right]$ provides a weighting of the differences. For each state, the difference is normalized with the locally occurring equivalent strain with

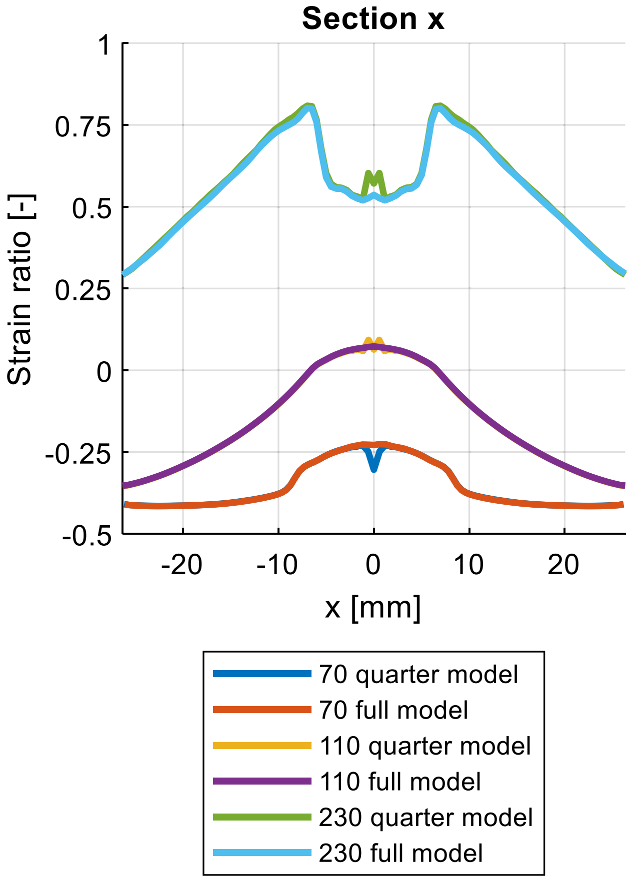

Fig. 34 Strain ratios along the section in *x*-direction (see Fig. 18) for the three specimen geometries each derived from the full and quarter models

respect to the highest occurring equivalent strain of the current state. This results in regions with higher equivalent strains being weighted more heavily. In the strain distributions, this corresponds to a stronger weighting of the outer regions. As a consequence, inner regions of the strain distribution, where comparatively large numbers of points are located, have less influence on the overall difference. Thus, more emphasis is placed on the characteristics of the strain distributions. Also with regard to the investigation of material models, it seems reasonable to give more weight to strongly hardened areas, since in the MUC-Test different material properties are significantly reflected in the characteristics of the strain distribution, cf. Figure 22.

If the sum in Eq. (3) is formed only over the states i, an average difference results for each material point. This difference can be shown spatially resolved in the *x*-*y*-plane (Fig. 28) or in the strain distribution (Fig. 29).

If the sum in Eq. (3) is calculated only over the nodes j, the result is a mean deviation for each stage. Figure 30 shows the evolution of this difference and the resulting

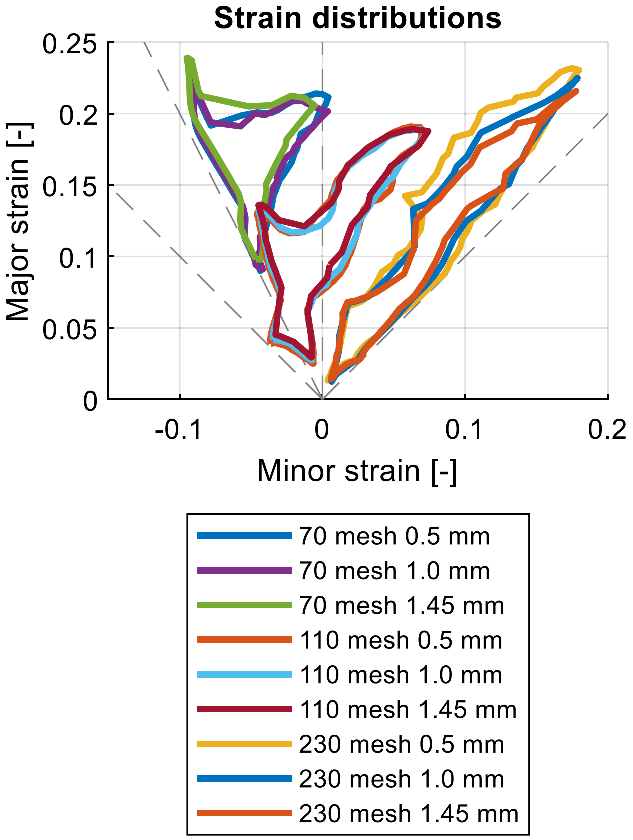

Fig. 35 Envelopes of the strain distributions for mesh sizes of 0.5 mm, 1.0 mm and 1.45 mm (Sim)

total difference according to Eq. (3) taking the major strain as an example. In this representation, it is possible to estimate how the difference behaves over the punch stroke and is thus an indication of the quality of the hardening behavior.

Comparison of Punch Forces

The comparison of the punch forces between reference and investigated data only requires a punch stroke dependent scalar comparison. Again, the Ref-data for the punch strokes under investigation in the Inv-data is determined by linear interpolation. The root mean square (RMS) according to Eq. (4) serves as a measure of the difference.

$$RMS_F = \sqrt{\frac{\sum_{i=1}^{k} \left({}^{i}F^{\mathrm{Inv}} - {}^{i}F^{\mathrm{Ref}}\right)^2}{k}} \tag{4}$$

Figure 31 shows an example of the progression of the punch force difference and the resulting total difference.

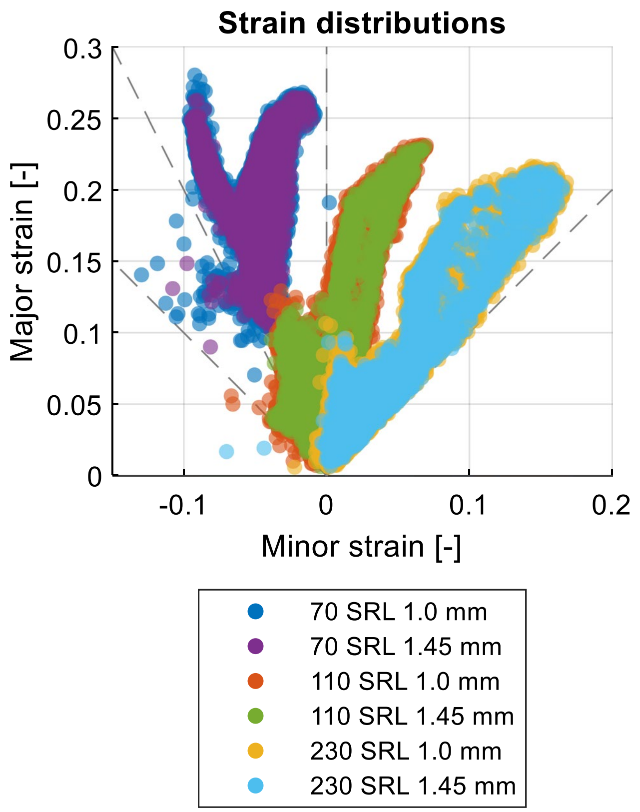

Fig. 36 Strain distributions for experiments using strain reference lengths (SRL) of 1.0 mm and 1.45 mm (Exp)

With the presented data comparison approach, it is possible to quantify differences between reference and investigation data and to evaluate them with scalar values. For each comparison, this results in three scalar values for the differences in major strain $\left(RMS_{\varepsilon_1}\right)$, minor strain $\left(RMS_{\varepsilon_2}\right)$ and punch force $\left(RMS_F\right)$.

Sensitivity Analyses

In this chapter, after a verification of the data comparison tool, different sensitivity analyses are performed. Initially, the numerical representation is examined by analyzing selected numerical parameters. Thus, the choice of numerical parameters can be verified. Subsequently, the influence of different process parameters on the result of the MUC-Test is investigated. The aim is to separate the influences of the process parameters from those of the material model parameters in order to allow a dedicated investigation of the material model. Finally, the influences of the material model parameters on the results of the MUC-Test are investigated and quantified.

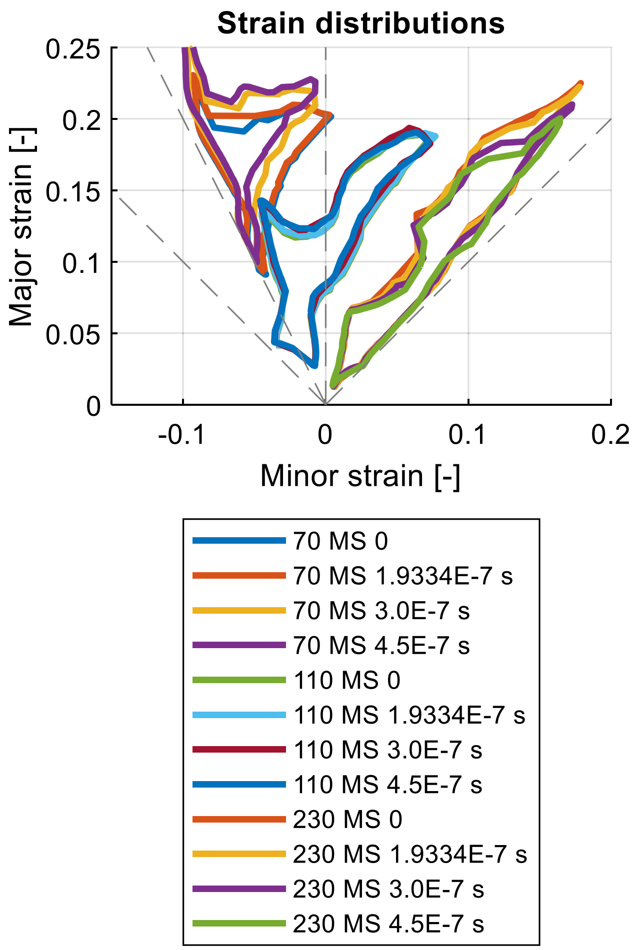

Fig. 37 Comparison of strain distributions (Sim) using different minimal time steps for mass scaling (MS)

The material model used for the parameter studies is the *Vegter06* model presented in the section Dual-phase steel DP590HD. For each parameter configuration, the three specimen geometries used (70 mm, 110 mm, 230 mm) are investigated with rolling direction at 0°. Unless explicitly mentioned, parameter values from the chapter *Setup of the numerical representation* are used.

Verification of the Data Comparison Tool

For verification of the evaluation tool, the differences resulting from using the same simulations as reference data and test data are analyzed. Figure 32 shows the resulting differences in major and minor strain and punch force for the three specimen geometries. The differences in the strains are in the magnitude of 10^{-20} and are thus negligible. For the punch force, a difference equal to zero results in each case. The evaluation tool can thus be rated as verified.

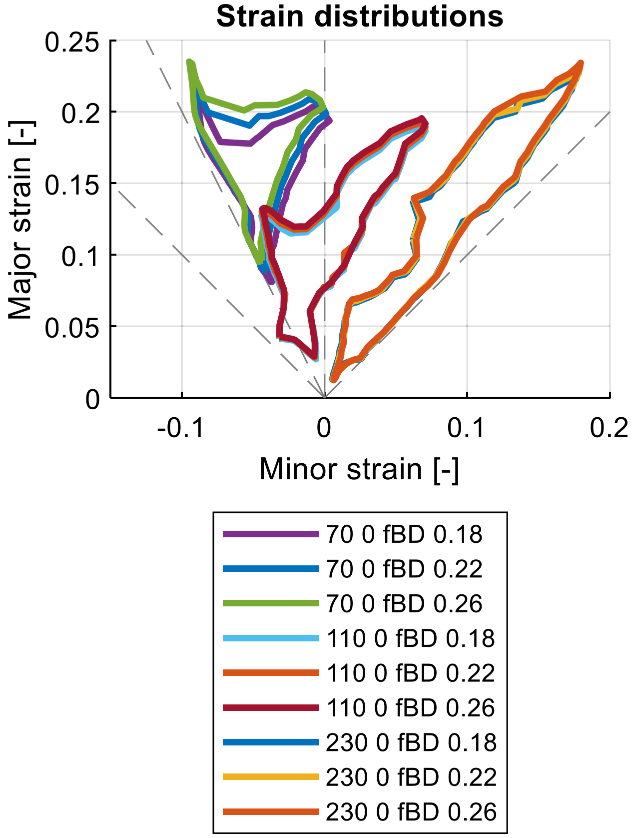

Fig. 38 Strain distributions (Sim) for different coefficients of friction for blankholder and die (fBD)

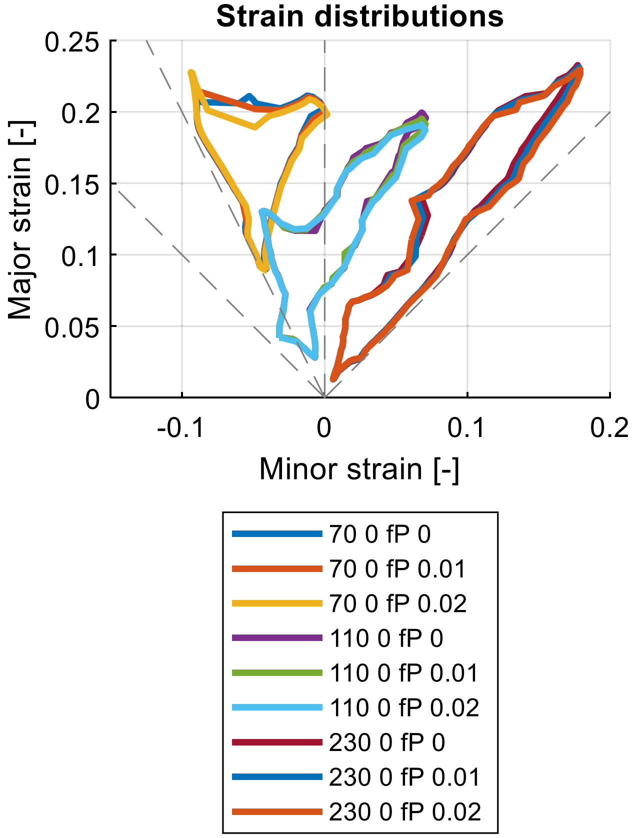

Fig. 39 Strain distributions (Sim) for different coefficients of friction for punch (fP)

Investigation of Numerical Parameters

In the next step, the numerical representation of the MUC-Test is examined for robustness with respect to numerical parameters. For this purpose, a simulation of comparatively fine resolution is used as a reference. For the meshing of the sample geometries a mesh size of 0.5 mm is chosen, mass scaling is not used and nine integration points over the sheet thickness are used.

Full Model – quarter Model

Figure 33 shows the envelopes of the simulative determined (Sim) strain distributions for quarter and full models. The strain characteristics of the two modeling types are essentially congruent. The visible differences arise especially at the marked points, which are due to the displacement boundary conditions at the symmetry planes. Due to these boundary conditions, numerical artifacts occur, which cause strains especially at the intersection of the symmetry planes. Figure 34 shows the strain ratios along the section in x-direction (see Fig. 18) for the three specimen geometries each derived from the full and quarter models. This shows that in the quarter model artifacts in the strains only occur at the intersection of the symmetry planes ($x = 0$). By reducing the model from a full model to a quarter model, the computation time is significantly reduced by a factor of 4.5. The difference in the strains, which can be classified as small, is acceptable with regard to the significantly reduced computation time.

Mesh Size

In order to determine a suitable mesh size for the specimen geometries, numerical investigations with mesh sizes of 0.5 mm, 1.0 mm, 1.45 mm, 2.0 mm and 3.0 mm are examined. For selected mesh sizes, the resulting differences in strain distributions are shown in Fig. 35. For the 70 mm specimen, a shift to the upper left results from a mesh size larger than 1.0 mm. A mesh with 1.0 mm edge length results in a comparable strain distribution to the reference mesh of 0.5 mm. Only in the strain region of the punch corners (characteristic point (1) in Figs. 18 and 19), strains are resolved less finely. For the 110 mm specimen, only minor differences are discernible; for the 230 mm specimen, the widening of the strain distribution decreases with increasing mesh size. Using a mesh size of 1.0 mm, the required computation time is reduced by a factor of 10 compared to the simulation with the reference mesh size of 0.5 mm. Based on these investigations, a mesh size of 1.0 mm is assumed to be an acceptable compromise between model accuracy and computation time and is specified as the mesh size for the following investigations.

As mentioned in the chapter *Test conditions*, a strain reference length (SRL) of 1.45 mm is used for the experiments. Consequently, the reference strain lengths between experiment and numerical representation differ from each other. To ensure that a comparison between experiment and numerical representation is nonetheless possible, the influence of the choice of reference strain length on the experimental results is investigated. Figure 36 shows that changing the strain reference length in the experiment only changes the density of the points, but not the shape of the strain distribution. In particular, the scattering of the data increases with decreasing strain reference length. It can be concluded that a reference strain length of 1.45 mm in the experiment compared to a reference strain length of 1.0 mm provides comparable strain distributions with less scattering and less data. Thus, a comparison between

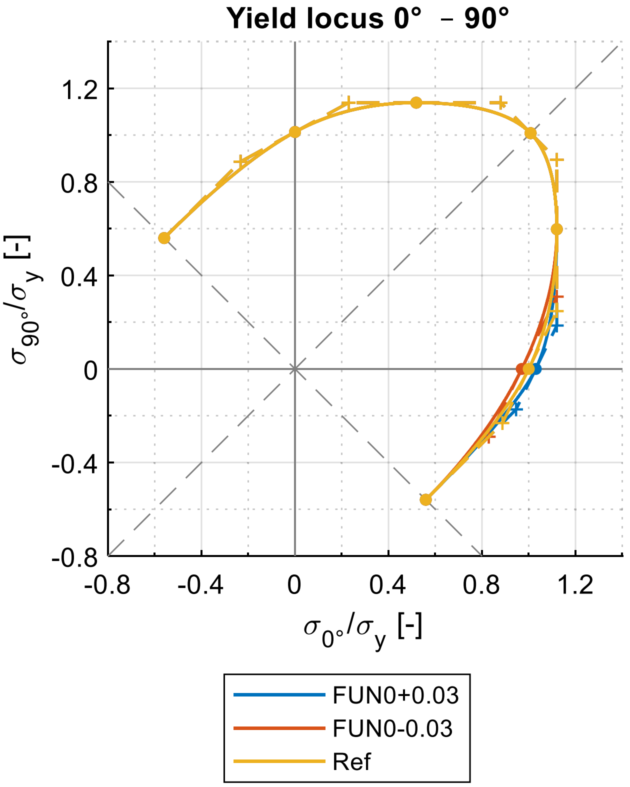

Fig. 40 Yield loci in the 0° – 90°-plane for a parameter variation of FUN0 ± 0.03 in comparison to the reference (Ref)

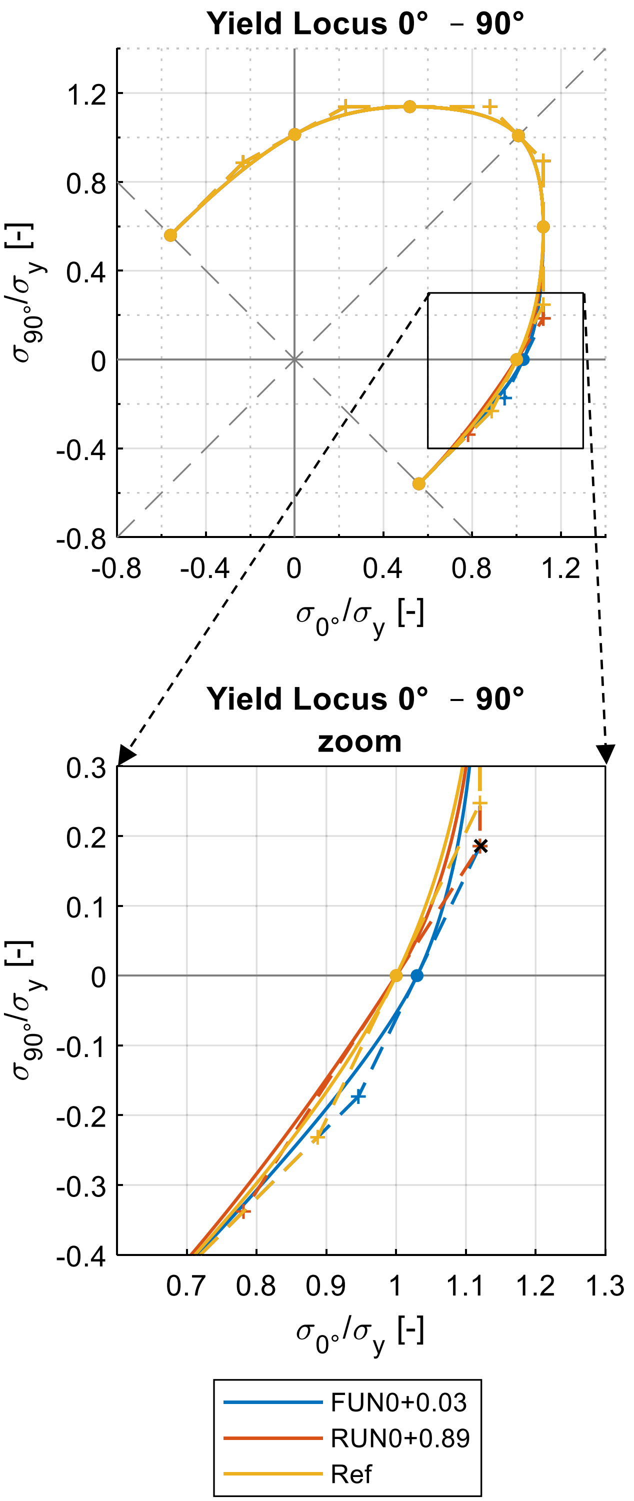

Fig. 41 Yield loci in the 0° – 90°-plane for parameter variations FUN0 + 0.03 and RUN0 + 0.89 in comparison to the reference (Ref) in total (upper part). The detail in the lower part of the figure shows the strategy of defining further parameter variations. The parameter RUN0 is changed in a way that the same hinge point as for the basic parameter variation of FUN0 + 0.03 is used (marked with a black cross)

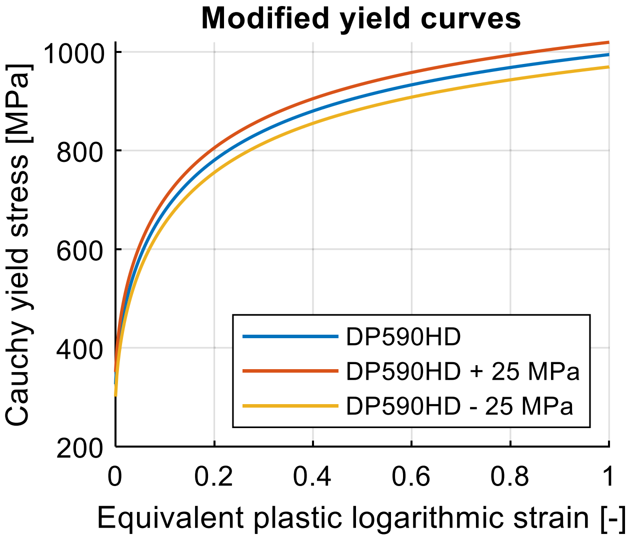

Fig. 42 Translation of the reference yield curve for parameter study

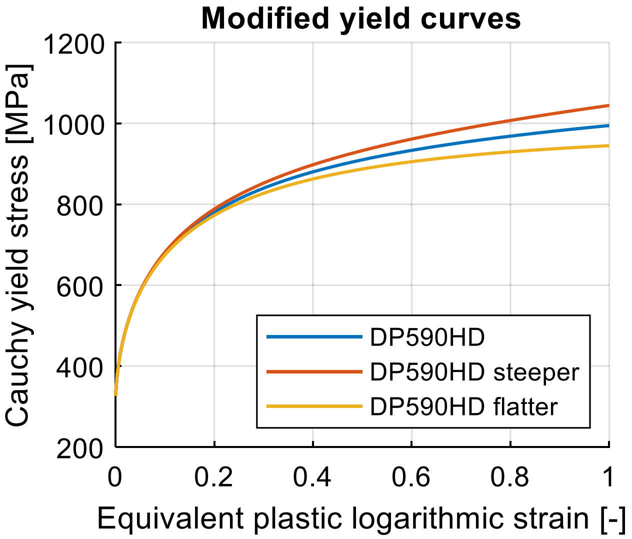

Fig. 43 Change in slope of the reference yield curve for parameter study

a numerical mesh size of 1.0 mm and an experimental reference strain length of 1.45 mm is valid and will be used in the following.

As part of the mesh study, the influence of the number of integration points over the sheet thickness was also investigated. No significant influence on the results of the numerical investigations was found. Therefore, the number of integration points was reduced from 9 to 5.

Mass Scaling

Simulations with different minimum time steps were run to find a suitable parameter for the mass scaling. For a mesh size of 1.0 mm, the Courant criterion results in a critical time step of $MS = 1.9334 \cdot 10^{-7}$ s for the material model used [45, 46]. In addition to this value, simulations with time steps of $MS = 3.0 \cdot 10^{-7}$ s, $MS = 3.5 \cdot 10^{-7}$ s, $MS = 4.0 \cdot 10^{-7}$ s and $MS = 4.5 \cdot 10^{-7}$ s were computed and compared with simulations without mass scaling. Exemplary resulting differences are shown in Fig. 37. Since the 70 mm sample in particular shows a strong dependence on the mass scaling, the following calculations are made without mass scaling.

Investigation of Process Parameters

After central numerical parameters have been investigated and determined, this chapter examines important process parameters with regard to their influence on the numerical results. Of particular interest is the influence of friction between the blankholder and the sheet, between the sheet and the die, and between the sheet and the punch. In this work, the Coulomb friction law is used. In the experiment, no lubrication is used between the specimens, the blankholder and the die. Consequently, these pairs of contacts are modeled with the same friction coefficient. Friction between sheet and punch is significantly reduced by the use of the selected lubrication concept, consisting of two-layer deep-drawing foil and lubricating paste, as can be seen in Fig. 21. Accordingly, for the following investigations, the friction between the specimens and the blankholder and die is modeled with a friction coefficient of $f_{BD} = 0.22$ and between the specimens and die with $f_P = 0.015$ in the reference configuration. The simulation model described in section Setup of the numerical representation serves as a simulation reference.

Friction of Blankholder and Die

The influence of the friction between the specimen and the blankholder as well as the die is illustrated by the strain distributions in Fig. 38. It can be seen that the 70 mm specimen in particular reacts sensitively to the friction modeling, in the form that the strain distributions are shifted upwards to the left as the coefficient of friction increases. The higher the friction in the area between blankholder and die, the more tangential force acts on the specimen in the contact area and the less deformation is possible in this area. Consequently, for

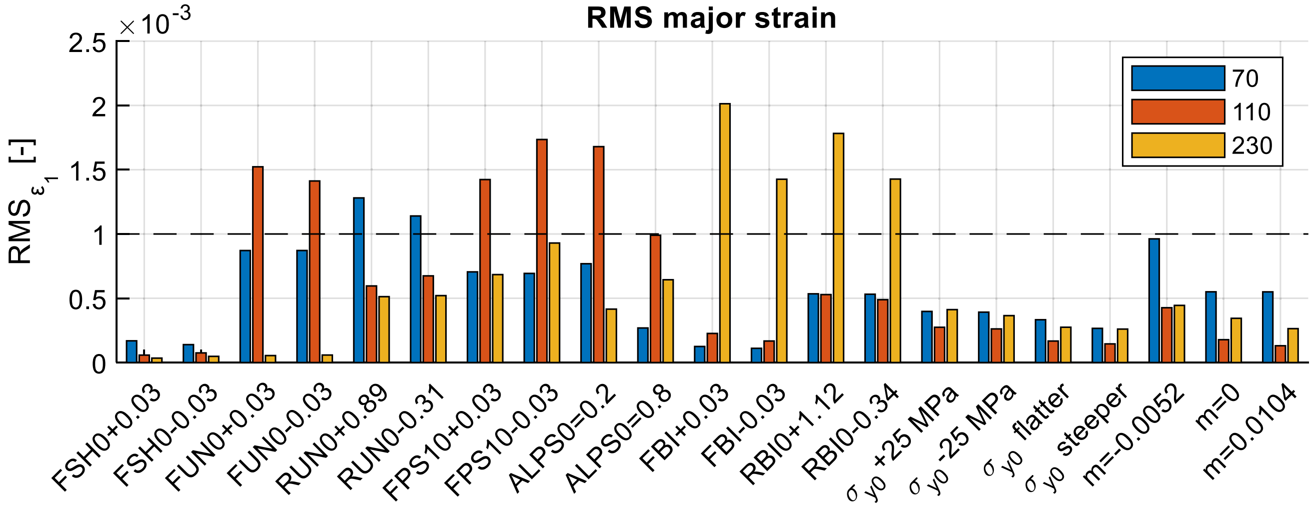

Fig. 44 Differences in major strain resulting from material model parameter studies. The horizontal dashed line shows the limit used to classify the differences

the same punch stroke, more forming must take place in the area not in contact with the blankholder and die. This results in the tendency shown in Fig. 38 that the strain distributions of the 70 mm specimen are shifted to higher strains towards the top left of the diagram as the coefficient of friction increases. As the specimen width increases, the potential relative motion between the blank and the tool or die decreases, making these specimen geometries less sensitive to friction. A strategy for calibrating friction is shown below in the section Modeling of friction.

Punch Friction

In the case of the punch, the aim was to reduce the friction between the punch and the sheet as much as possible. Qualitatively, it was shown in Fig. 21 that the strain distributions depend on the punch friction. This was compared experimentally by comparing the selected lubrication concept with lubrication using deep drawing oil. It can be assumed that these two lubrication concepts result in significantly different friction values. Accordingly, the following investigations are shown for a range

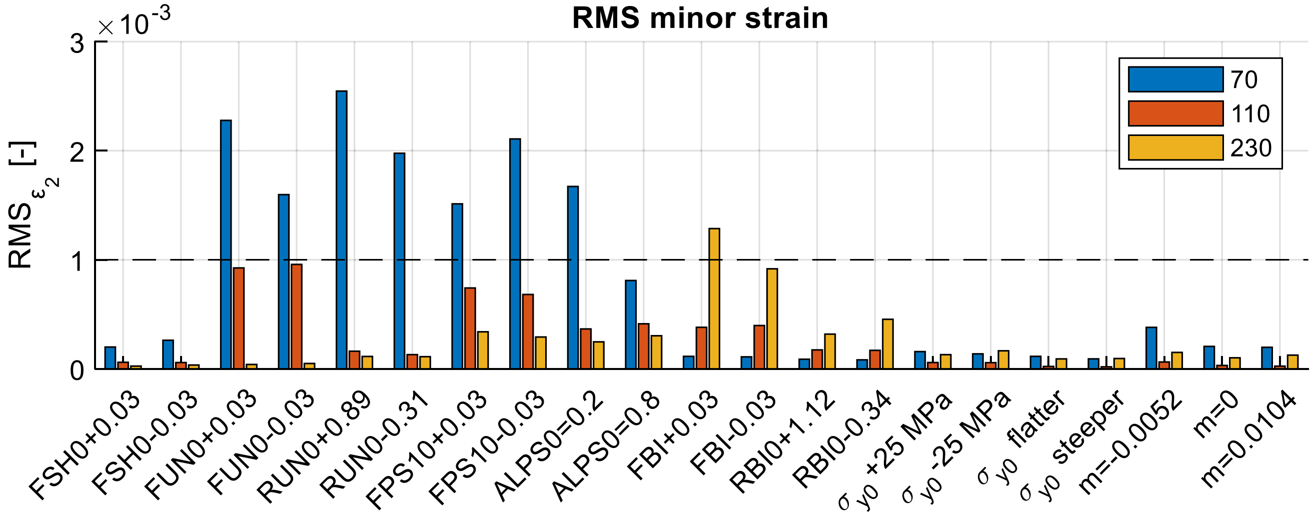

Fig. 45 Differences in minor strain resulting from material model parameter studies. The horizontal dashed line shows the limit used to classify the differences

of comparatively small coefficients of friction, which appear reasonable for the selected lubrication concept. Figure 39 shows that the strain distributions in the investigated friction coefficient range do not depend strongly on the friction between specimen and punch. One way of calibrating the punch friction is explained in the section Modeling of friction.

Investigation of Material Parameters

After the simulation has been examined with regard to numerical and process parameters and the different influencing factors have been shown, the influence of the material model parameters on the result of the FE simulation can now be examined. This represents an essential step towards understanding the MUC-Test and is thus the basis for the subsequent validation.

In the following, important parameters of the material model are investigated. On the one hand, the yield curve is modified by changing its slope $\left(\sigma_{y0}\ \text{steeper}, \sigma_{y0}\ \text{flatter}\right)$ and its absolute position $\left(\sigma_{y0} \pm 25\ \text{MPa}\right)$ as well as by changing the strain rate dependency (m). On the other hand, the yield locus parameters (FSH0, FUN0, RUN0, FPS10, ALPS0, FBI, RBI0, cf. Figure 3) are systematically varied. The variation of the parameters is chosen in such a way that the degree of change of the yield locus corresponds in each case. This allows a qualitative as well as a quantitative comparison of the influences of the model parameters on the numerical result.

The absolute values of the parameter changes are determined by a change of 0.03 in the normalized stress values. As shown in Fig. 40, this results in a clear but moderate change in the yield locus.

The comparability of the parameter variations is realized by changing different parameters always resulting in the same changes of the hinge points. The procedure is explained at the example of the parameter RUN0 based on the change of FUN0 + 0.03. Due to the specified change in the parameter FUN0 by + 0.03, two changed hinge points result, both of which move closer to the uniaxial tension point, cf. Figure 40. The parameter RUN0 influences the tangent at the uniaxial tension point FUN0. When the parameter RUN0 is changed, one hinge point thus moves closer to the uniaxial tension point, the other hinge point moves in the opposite direction. The parameter RUN0 is now changed in such a way that the hinge point, which lies in the area between uniaxial and biaxial tension, has the same coordinates as when the parameter FUN0 is changed by + 0.03. This results in a change of + 0.89 for RUN0. This is illustrated graphically in Fig. 41. All further parameter changes are derived accordingly. When changing the parameter ALPS0, the hinge points do not change. In this case, the parameter was set to the values 0.2 and 0.8.

In the yield curve, the factor of 0.03 used above results in a value of about 25 MPa at uniform elongation, which is used as the absolute value for the yield curve displacement, see Fig. 42. The flatter or steeper yield curve was chosen so that the selected extrapolation approaches can be used reasonably, see Fig. 43. The parameter of the strain rate dependency m is doubled starting from the reference value, set to zero and negative.

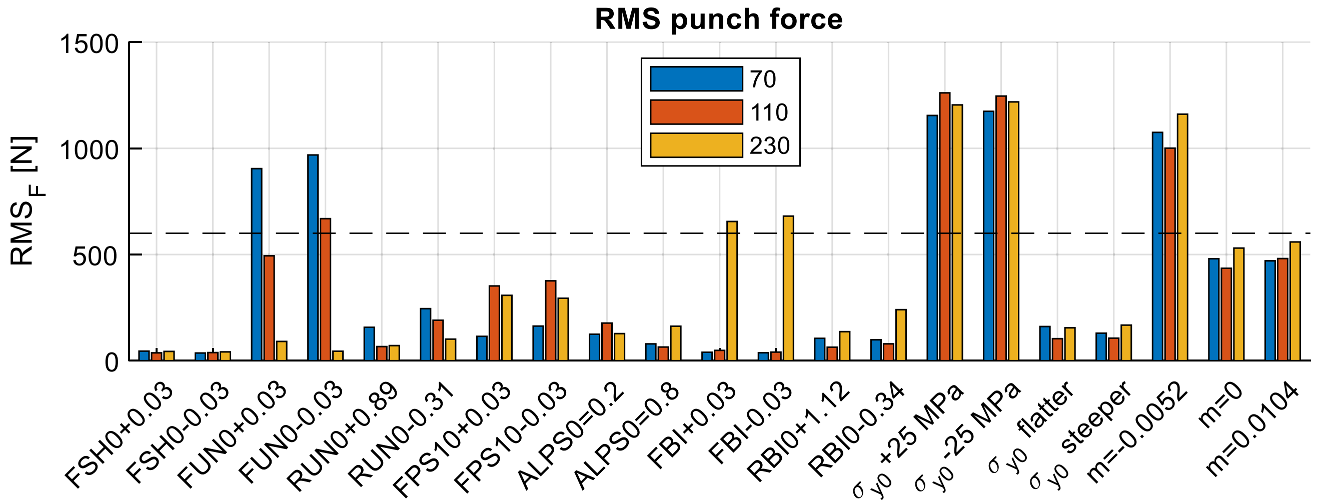

Fig. 46 Differences in punch force resulting from material model parameter studies. The horizontal dashed line shows the limit used to classify the differences

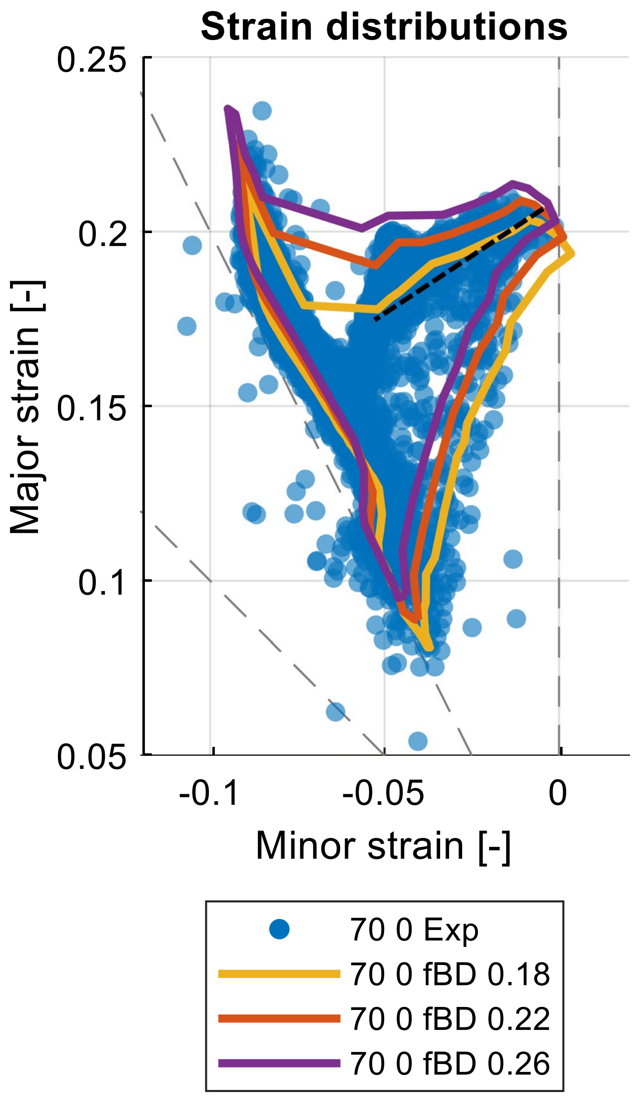

Fig. 47 Experimental strain distribution (Exp) in comparison to envelopes of strain distributions resulting from numerical analyses (Sim) using different coefficients of friction for the contacts between specimen and blankholder and die (fBD). A value of $f_{BD} = 0.22$ represents the mid-position of the experimental strain distribution (dashed line) best and is used for further analyses

The diagrams of the strain distributions resulting from the changes of the material model parameters are shown in the appendix *Strain distributions for material model parameter study*. In addition to this purely visual comparison, the parameter studies were evaluated using the data comparison tool presented in section Data comparison approach. The resulting differences for major strain $\left(RMS_{\varepsilon_1}\right)$, minor strain $\left(RMS_{\varepsilon_2}\right)$ and punch force $\left(RMS_F\right)$ are summarized in Figs. 44, 45 and 46.

The resulting differences shown in the figures can now be classified according to the parameter influence. For major and

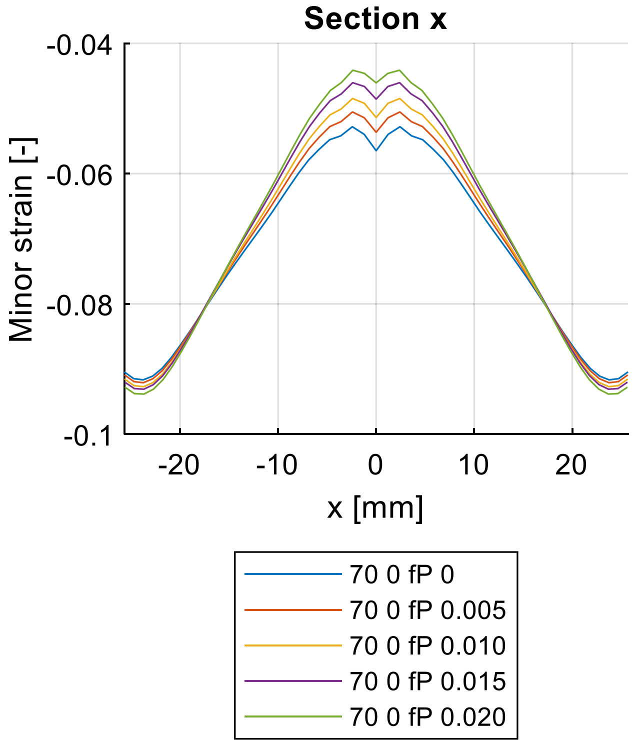

Fig. 48 Influence of different coefficients of friction for the contact between sheet and punch (fP) on the minor strains along the section along the section *x* (Sim)

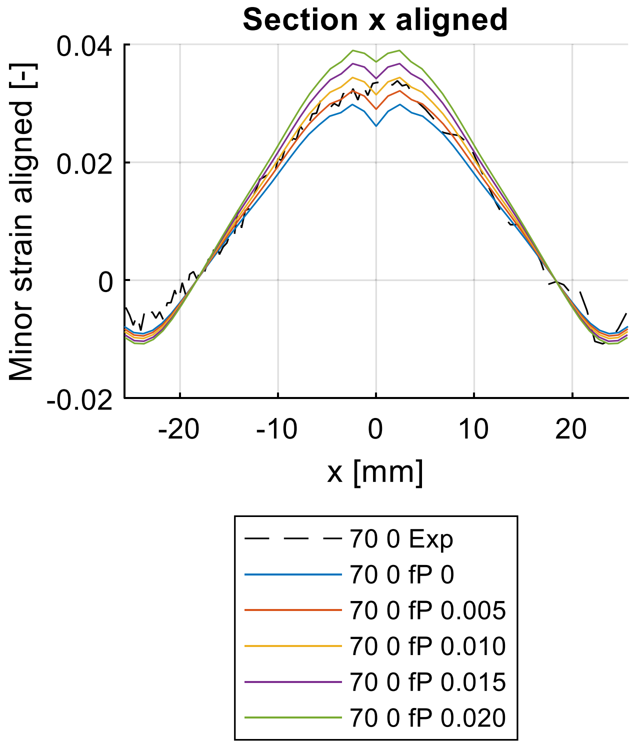

Fig. 49 Minor strains along the section *x* aligned at the anchor point for numerical analyses (Sim) using different coefficients of friction for the contact between sheet and punch (fP) and a representative experiment (Exp)

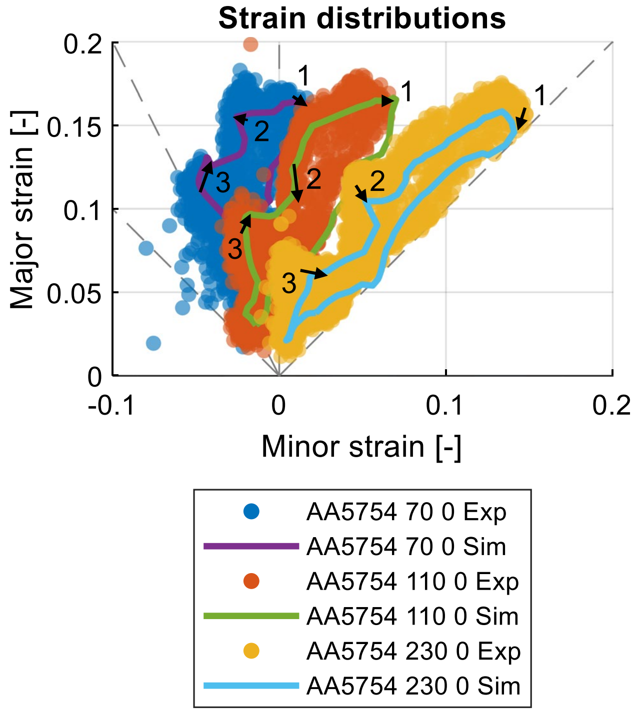

Fig. 50 Strain distributions resulting from experiments (Exp) with the aluminum alloy AA5754 in comparison to envelopes of the numerical representations (Sim). The arrows indicate the change of the characteristic points (1: punch corner, 2: punch center, 3: flange, cf. Figure 18) from the experiments to the numerical results (Exp ➔ Sim)

minor strain, a limit of $\mathrm{Lim}\left(RMS_{\varepsilon_{1,2}}\right) = 1.0 \cdot 10^{-3}$ is defined. For differences in punch force, the limit is set to $\mathrm{Lim}\left(RMS_F\right) = 600$ N. Parameters leading to differences that are above Lim are classified into the group of parameters with large influence. By this classification, it is possible to compare the different values quantitatively and to add them up to a total difference RMS_{total} according to the following Eq. (5). Therein, the reciprocals of the limits were used as weights w between the several differences. This gives an approximately equal weighting to the differences in the strains and the stresses.

$$RMS_{\mathrm{total}} = w_{\varepsilon_1} \cdot RMS_{\varepsilon_1} + w_{\varepsilon_2} \cdot RMS_{\varepsilon_2} + w_F \cdot RMS_F \tag{5}$$

where

$$\begin{aligned} w_{\varepsilon_1} &= \left(\mathrm{Lim}\left(RMS_{\varepsilon_1}\right)\right)^{-1} \\ w_{\varepsilon_1} &= \left(\mathrm{Lim}\left(RMS_{\varepsilon_2}\right)\right)^{-1} \\ w_F &= \left(\mathrm{Lim}\left(RMS_F\right)\right)^{-1} \end{aligned} \tag{6}$$

Equation (5) makes it possible for both, parameter studies (comparison of two simulations) and validations (comparison of an experiment with a simulation) to quantify the corresponding total difference by means of one single scalar, which can be used as a basis for material model validation.

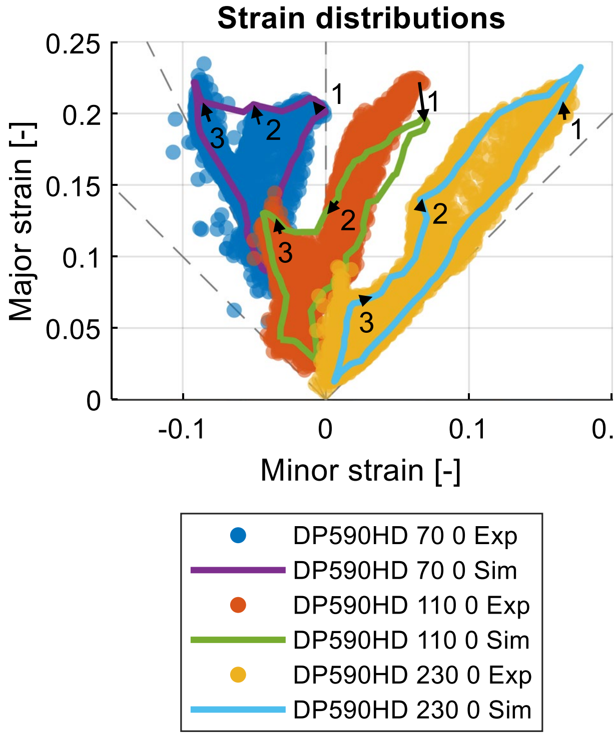

Fig. 51 Strain distributions resulting from experiments (Exp) with the dual-phase steel DP590HD in comparison to envelopes of the numerical representations (Sim). The arrows indicate the change of the characteristic points (1: punch corner, 2: punch center, 3: flange, cf. Figure 18) from the experiments to the numerical results (Exp ➔ Sim)

Modeling of Friction

Before investigations of the material model can be performed using the MUC-Test, it must be ensured that the numerical representation does not depend significantly on numerical parameters and process parameters. Based on the investigations shown so far, this chapter presents a strategy for calibrating the friction. If the friction is sufficiently modeled, the numerical model of the test is significantly dependent only on material model parameters, which makes validation of the same reasonably possible.

Friction of Blankholder and Die

The parameter studies show that the strain distribution of the 70 mm specimens with variable friction between blank and blankholder or die in the principal strain space show a shift to the upper left, cf. Figure 38. A comparison with the other parameter studies shows that this dependence does not apply to any other parameter. This allows a phenomenological calibration of the friction model between sheet and blankholder or die.

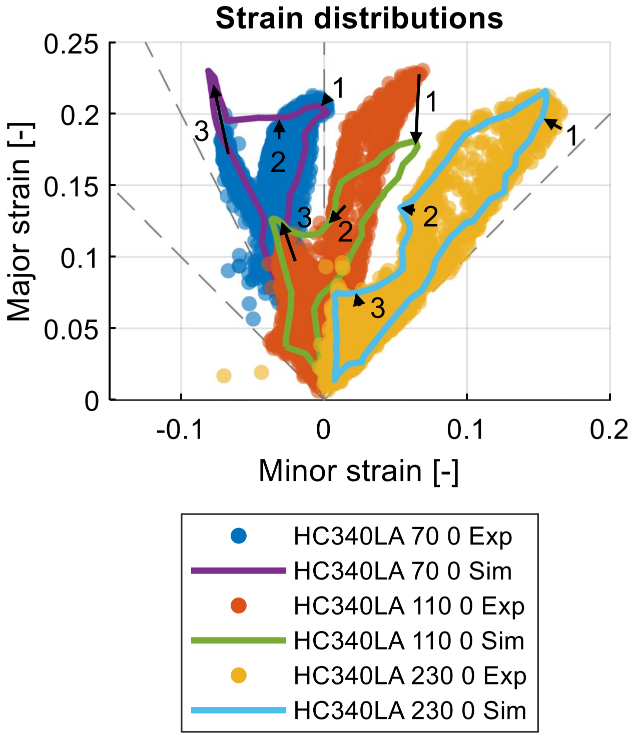

Fig. 52 Strain distributions resulting from experiments (Exp) with the microalloyed steel HC340LA in comparison to envelopes of the numerical representations (Sim). The arrows indicate the change of the characteristic points (1: punch corner, 2: punch center, 3: flange, cf. Figure 18) from the experiments to the numerical results (Exp ➔ Sim)

This phenomenon can be reduced to the condition that the friction is adequately modeled if the axis of the right branch of the strain distribution (dashed line in Fig. 47) is in good alignment with the experiment. For the DP590HD material, the friction calibration is shown as an example in Fig. 47. From this representation, the friction coefficient of the contacts between blank and blankholder and blank and die is $f_{BD} = 0.22$.

Punch Friction

Figure 39 shows that for the relevant friction forces, the modeling of the friction between punch and sheet has little influence on the result of the MUC-Test. Nevertheless, a method is presented here by means of which it is possible to adjust this friction pairing finely. Evaluations of the parameter studies showed that the minor strain along the section in the x-direction is suitable for this calibration. The minor strains shown in Fig. 48 have an anchor point around which the strains rotate along the cut. This anchor point is at $x = \pm 18.3$ mm for the DP590HD material. This behavior is not shown by any other parameter investigated and thus can be used to calibrate the punch friction. However, since other parameters cause a translation of the curve in ordinate direction, for the friction calibration all sections are shifted in ordinate direction so that they intersect the abscissa at the anchor point, cf. Figure 49. Thus, only the rotation around the anchor point remains as a degree of freedom, which can be used to calibrate the friction between blank and punch. From Fig. 49, a value of $f_P = 0.005$ is determined as suitable. The minima of the sections at $x = 0$, which can be seen in Figs. 48 and 49, are due to the symmetry boundary condition of the quarter model, which has already been discussed in the section Full model – quarter model (see Fig. 34).

Validation of the Investigated Material Models

Validation of the Material Models for AA5754, DP590HD and HC340LA

For each of the materials investigated, experiments were carried out with three specimen geometries (70 mm, 110 mm, 230 mm) in three rolling directions (0°, 45°, 90°) and with three repetitions. This results in nine configurations per material, which are numerically simulated and evaluated by applying the data comparison tool shown in section Data comparison approach regarding their differences with respect to the experimental reference.

For the simulations of the MUC-Test with the aluminum material AA5754, the material model described in section Aluminum AA5754 is used. The friction between specimen and blankholder or die is modeled with a friction coefficient of $f_{BD} = 0.34$ using the method shown, and the friction between sheet and punch with $f_P = 0.02$. Figure 50 shows an example of a comparison of the strain distributions from experiment and simulation for the tests of the specimen geometries with rolling direction 0°.

The numerical representation of the MUC-Test with the dual-phase steel DP590HD is realized using the material card from the section Dual-phase steel DP590HD. The coefficient of friction between specimen and blankholder or die is set with a value of $f_{BD} = 0.22$, the coefficient of friction for the contact pair sheet and punch with $f_P = 0.005$. In Fig. 51, strain distributions of the numerical representation are compared with the experimental reference.

The MUC-Test for microalloyed steel HC340LA is numerically simulated using the material model shown in section Microalloyed steel HC340LA. The friction between specimen and blankholder or die is modeled according to the method in chapter *Modeling of friction* with a coefficient of friction of $f_{BD} = 0.34$, the friction between sheet and punch with a coefficient of friction of $f_P = 0.005$. In Fig. 52, the

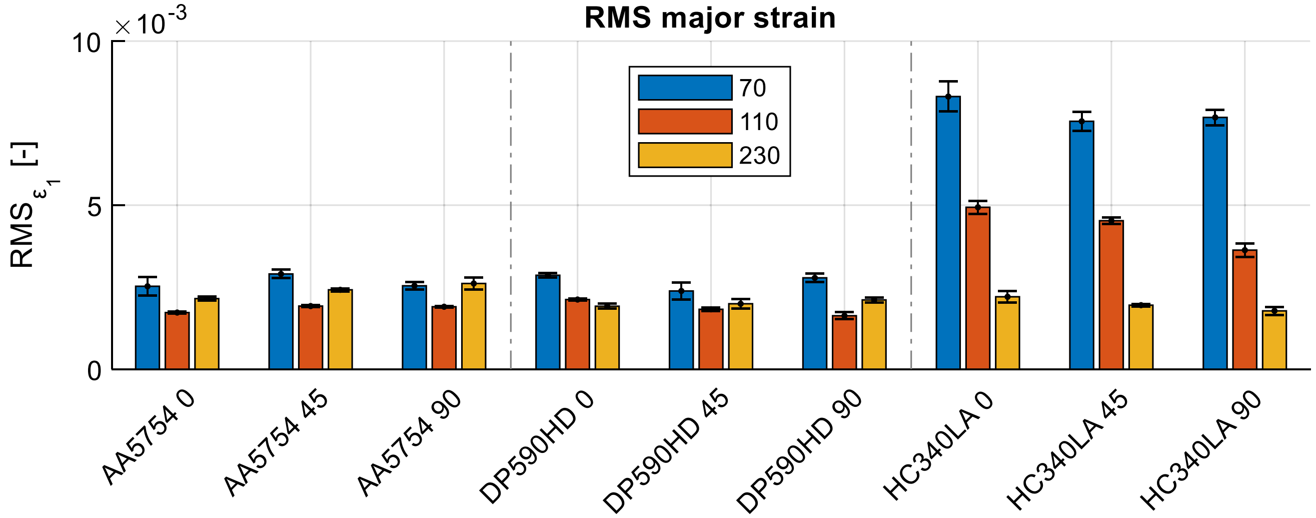

Fig. 53 Differences in major strain for the investigated materials AA5754, DP590HD and HC340LA

strain distributions from experiment and numerical representation are shown as an example.

The following figures (Figs. 53, 54, 55 and 56) show the results of the evaluation of the data comparison approach. Based on the threefold repetition of each experiment type, it is possible to determine a mean difference (bar height) and the standard deviation (error bar) between the experiments and the numerical representations for each category. From the individual differences for major strain $\left(RMS_{\varepsilon_1}\right)$, minor strain $\left(RMS_{\varepsilon_2}\right)$ and punch force $\left(RMS_F\right)$, a total difference $\left(RMS_{\text{total}}\right)$ can be determined according to Eq. (5).

The results show that for the major strain (Fig. 53), in particular the material model of the material HC340LA for the narrow specimen geometries shows large differences compared to the experiment. This is also reflected in the exemplary overlay of the strain distributions for one stage in Fig. 52. In the case of the minor strain (Fig. 54), the 230 mm sample of aluminum is particularly noticeable, resulting in comparatively large differences. This is due to the too small strain distribution in abscissa direction in the numerical representation, cf. Figure 50. In addition, the 70 mm specimens of HC340LA show increased differences in the minor strain to the experiment.

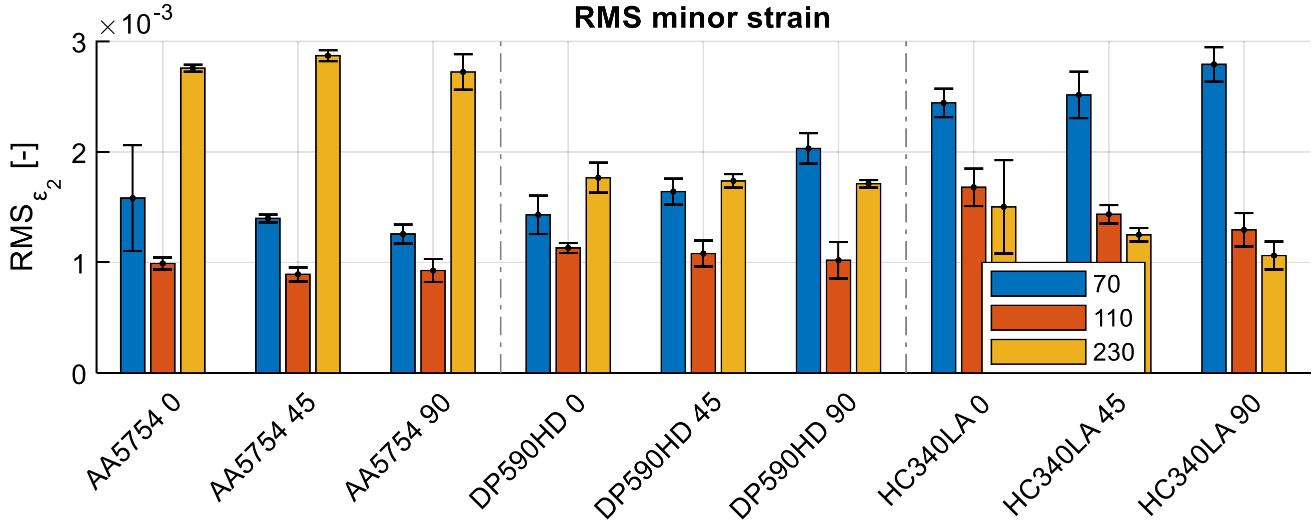

Fig. 54 Differences in minor strain for the investigated materials AA5754, DP590HD and HC340LA

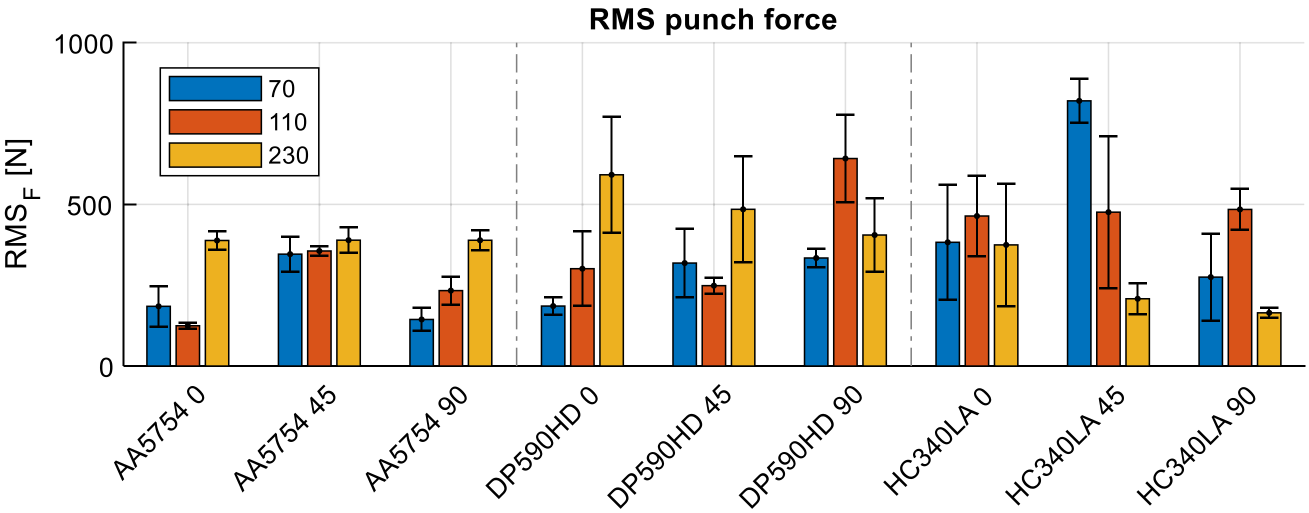

Fig. 55 Differences in punch force for the investigated materials AA5754, DP590HD and HC340LA

The comparison of the punch forces (Fig. 55) shows that these are comparatively well reproduced for the aluminum material. For the other materials, there are increased differences for individual specimens.

The overview of the total difference (Fig. 56), calculated according to Eq. (5), shows that in the case of the aluminum and the dual-phase steel, the 110 mm specimens show the smallest differences for all rolling directions compared to the other specimen geometries. The differences of the 70 mm and 230 mm specimens are of comparable magnitude. The mean value of the total differences for both materials also gives comparable values (total difference aluminum: 1.50, total difference dual-phase steel: 1.45). Significantly larger discrepancies can be observed for the microalloyed steel HC340LA. The total difference of 2.39 is mainly due to large differences in the 70 mm specimen geometries. The 110 mm specimens also show significantly larger differences compared to the other materials. These differences are mainly due to differences in the major strain.

Based on this evaluation, a validation in the form of a qualitative comparison between the materials is possible. Thus, the quality of the material model for the dual-phase steel DP590HD can be evaluated as better compared to the material model of the aluminum material AA5754

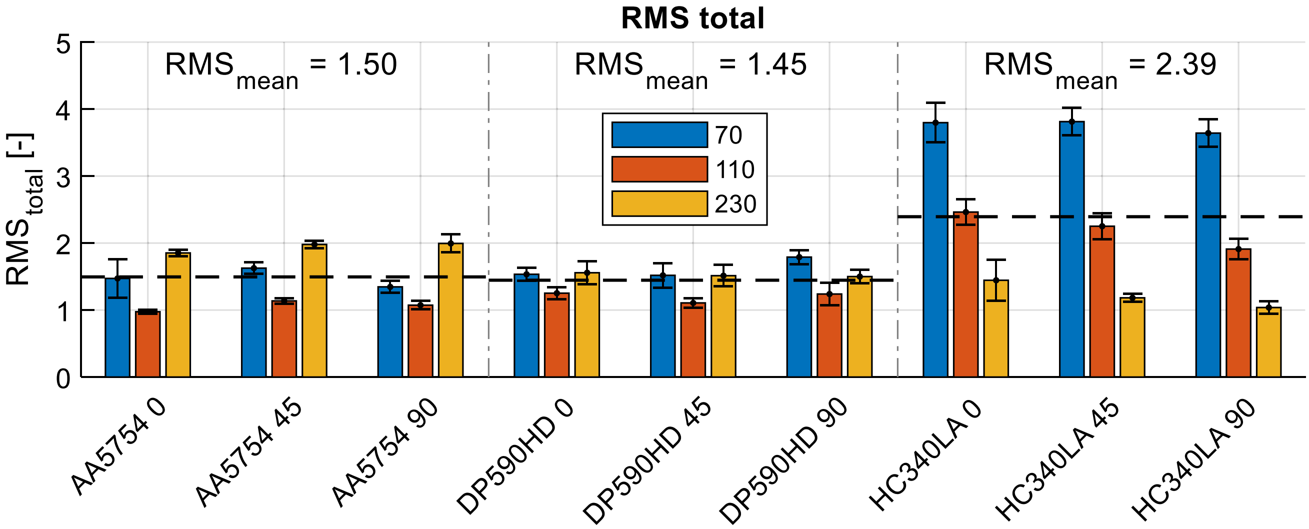

Fig. 56 Total differences for the investigated materials AA5754, DP590HD and HC340LA and averaged values for each material

Table 6 *Yld2000* parameters for the material DP590HD based on the material properties described in section Dual-phase steel DP590HD

Parameter	Value
α_1	0.9556
α_2	1.0406
α_3	1.0505
α_4	0.9811
α_5	0.9969
α_6	0.9432
α_7	0.9696
α_8	0.9978

and significantly better than that of the microalloyed steel HC340LA.

DP590HD with Different Material Models

In addition to the investigation of different materials, it is also of interest to what extent different material models vary in terms of modeling accuracy. For this purpose, the *Vegter06* model was calibrated to represent the yield locus description according to *Hill48* calibrated using anisotropy coefficients (*Vegter based on Hill48*) and stress ratios (*Vegter based on Hill48 SR*). In addition, the *Yld2000* yield locus model is used, which provides a comparable description to the *Vegter06* model calibrated based on the *BBC* model (*Vegter based on BBC M6*). With these four yield locus descriptions, the MUC-Test was numerically represented. The parameters from the section Dual-phase steel DP590HD were used to calibrate the models. For the *Yld2000* yield locus model, this results in the model parameters shown in Table 6.

The yield loci in comparison are shown in Fig. 57. Due to the same data basis and equivalent degrees of freedom, the yield locus descriptions *Yld2000* and *Vegter based on BBC M6* are congruent.

Because of the calibration in the stress space, the model *Vegter based on Hill48 SR* is congruent with the models *Yld2000* and *Vegter based on BBC M6* for uniaxial and equibiaxial tension. Differences arise in the interpolation between these calibration points. The model *Vegter based on Hill48* is calibrated in the strain space and shows larger differences in the stress space. It is expected that the models, which are calibrated in the stress space, result in a more realistic representation of the occurring stresses. According to the results from chapter *Investigation of material parameters* (Fig. 46), this is expected to result in a better representation of the punch forces for these models compared to the model *Hill48*. The resulting overall differences between the different models and the experiments are summarized in Fig. 58. The overview shows that the more complex models *Vegter from BBC M6* and *Yld2000* allow a more realistic representation than the less complex material

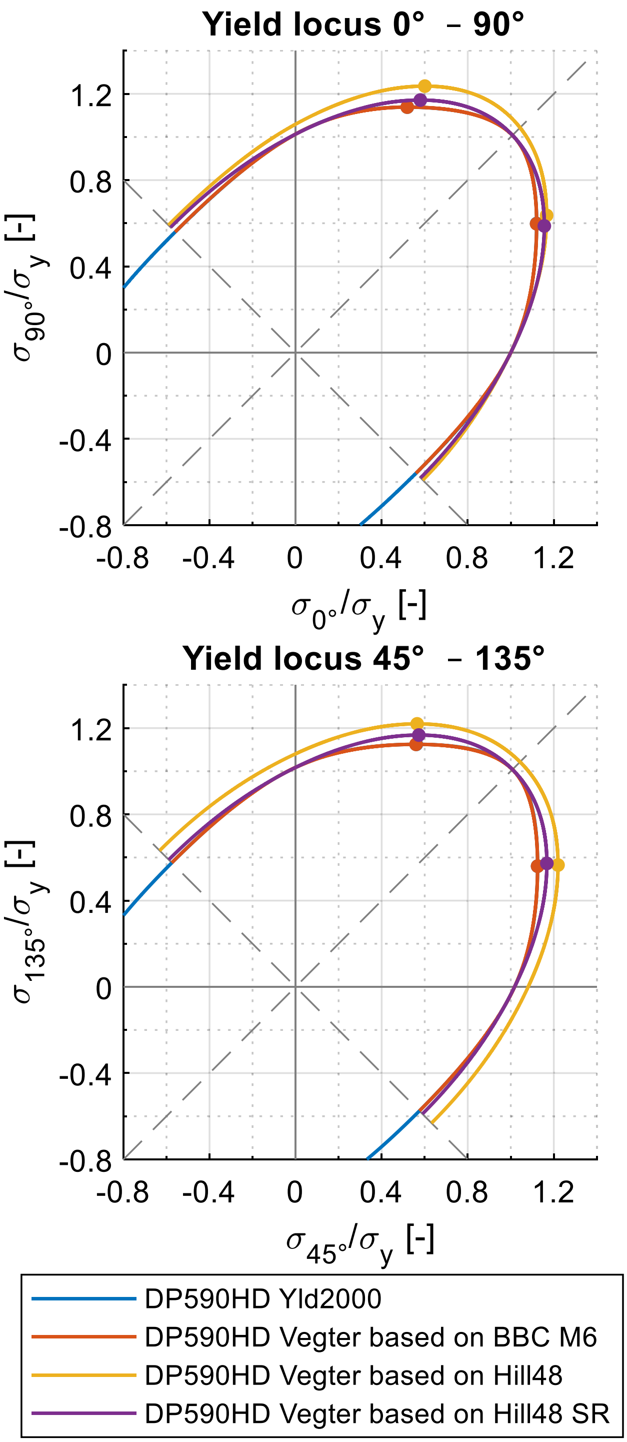

Fig. 57 Yield loci for the material DP590HD using different material models based on the material parameters presented in section Dual-phase steel DP590HD

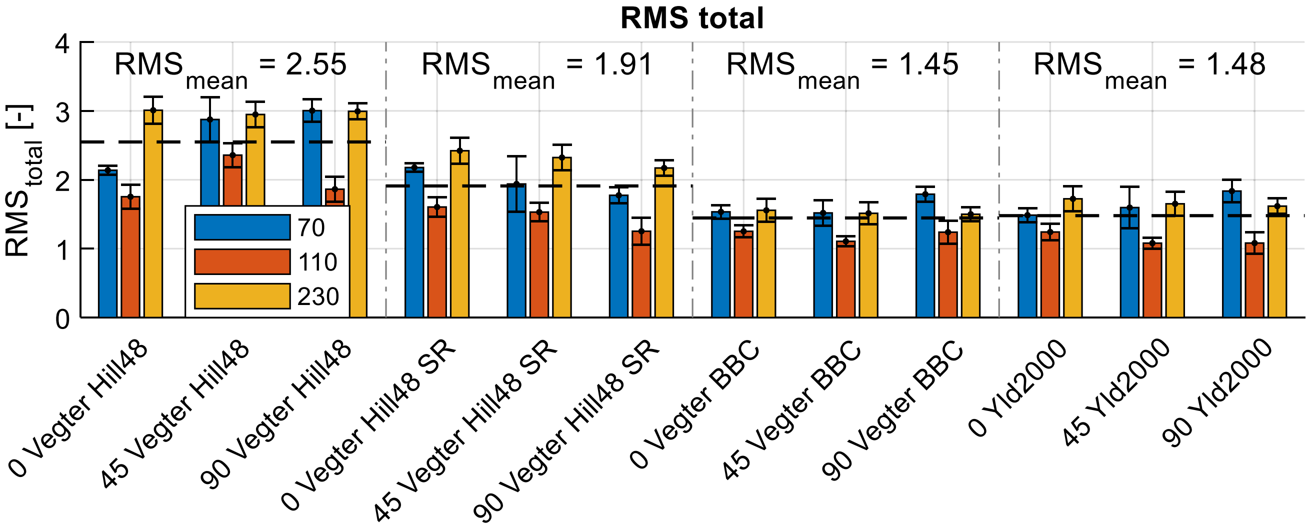

Fig. 58 Resulting total differences for the different material models for DP590HD and their averaged values

models. In the present case, the material model *Hill48 SR* leads to smaller overall differences than the *Hill48* model, since mainly the punch forces are represented much better, as expected. This shows a potential of this approach. In the chapter *Introduction* it was already mentioned that the challenge is to find a model, which is as simple as possible, but sufficiently accurate. It is essential how high the requirements for the individual factors of the model accuracy are. According to these requirements, the weights $w_{\varepsilon_{1,2},F}$ can be changed to represent the desired model accuracy. For example, if more emphasis is placed on accurately representing strains compared to representing forces, w_F can be reduced accordingly.

DP590HD Using Different Calibration Strategies

Another benefit of the presented material model validation method is that equivalent models calibrated in different ways can be compared. In this chapter, the material model of the dual-phase steel DP590HD from the chapter *Dual-phase steel DP590HD* is compared with two alternative models determined for the same batch of the material. The two alternative material models are based on a *BBC* model and on a *Yld2000* model. A comparison of the yield loci is shown in Fig. 59. The main differences are in the equibiaxial region and in the position of the points under plane strain. The resulting differences between the numerical representations of the MUC-Test using these material models compared to the experiments are shown in Fig. 60. The evaluation shows that the material model shown in section Dual-phase steel DP590HD is on average most capable of representing the real material behavior.

Summary and Outlook

In this work, an experiment tool has been presented that can be used to provide a comprehensive database for effective and efficient validation of material models: the MUC-Test (acronym for Material Under Control). This test fulfills the general requirements for a validation test of continuous data acquisition, simple test procedure, low number of tests required, a non-friction dominated test and complex strain distributions. In addition, it was shown that the test provides reproducible results and represents varying material properties.

The validation strategy of material models is based on a comparison of experimental results in terms of major and minor strain and punch force with a numerical representation of the MUC-Test. This digital twin was set up in the form of a FE simulation in LS-DYNA. For the comparison between the experimental and numerical data, a data comparison approach was presented which compares major and minor strains in the entire observable range based on a full-field comparison over the entire test run and derives differences. The differences in punch forces are quantified using a comparable measure. Using this data comparison tool, extensive parameter studies were carried out to investigate numerical parameters,

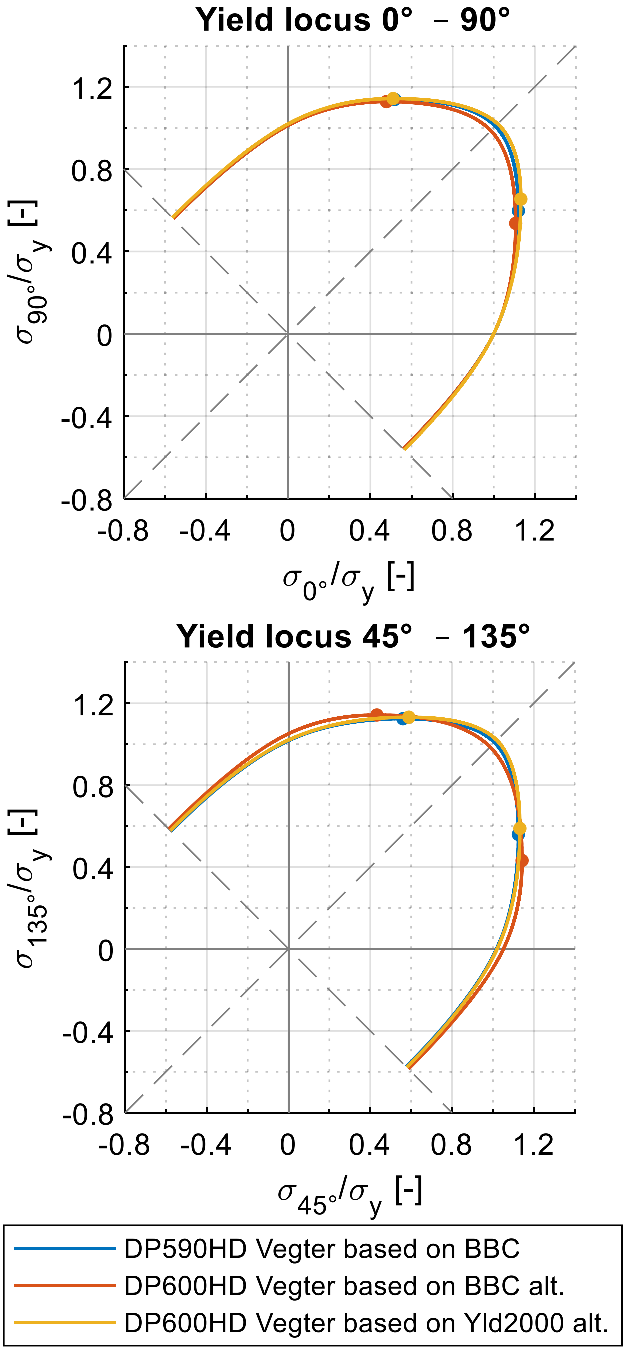

Fig. 59 Yield loci for DP590HD based on different calibration strategies

process parameters and material model parameters for their influence on the results of the MUC-Test. Based on the parameter studies, a phenomenological strategy for friction calibration was derived on the one hand. On the other hand, a weighting between the differences in major strain, minor strain and punch force, which allows determining one single scalar value as a measure for the total difference, was deduced.

The presented method for validation of material cards was performed for three materials of different material classes: The aluminum AA5754, the dual-phase steel DP590HD and the microalloyed steel HC340LA. This showed that the method can be used for different material classes. Furthermore, different models based on the same database were compared for the dual-phase steel DP590HD, showing the potential to identify suitable material models for specific requirements. Finally, equivalent material models based on different calibration strategies were compared. In conclusion, it was shown that the MUC-Test can be used to evaluate and compare different material models in terms of their ability to represent real material behavior. This evaluation is based on different physical quantities and uses a large extent of the performed punch stroke and thus of the forming history, which originates the effectiveness of the MUC-Test strategy.

Based on the presented method, further materials of different material classes will be investigated in order to generate a more comprehensive database for the evaluation of the method. In addition, it is possible to investigate further components of the material models. In this work, only isotropic yield locus hardening was used. For industrial processes with multistage forming steps, a pure isotropic hardening model can be a limiting factor for the realistic representation of the processes. Especially for nonlinear forming histories, more complex hardening models are necessary for an adequate numerical representation. Here, the MUC-Test can be used as a basis for model validation. For this purpose, specimens with different pre-strains can be post-strained using the MUC-Test. With the help of the presented evaluation tool, the accuracy of the representation and thus the quality of the modeling can then be validated for different modeling approaches.

The presented data comparison tool allows an evaluation of the model quality for different parameter configurations. This can be used to find parameters for which the difference between experiment and the numerical representations becomes smaller. Consequently, the MUC-Test in combination with the tool for the data comparison provides the basis for a material model optimization.

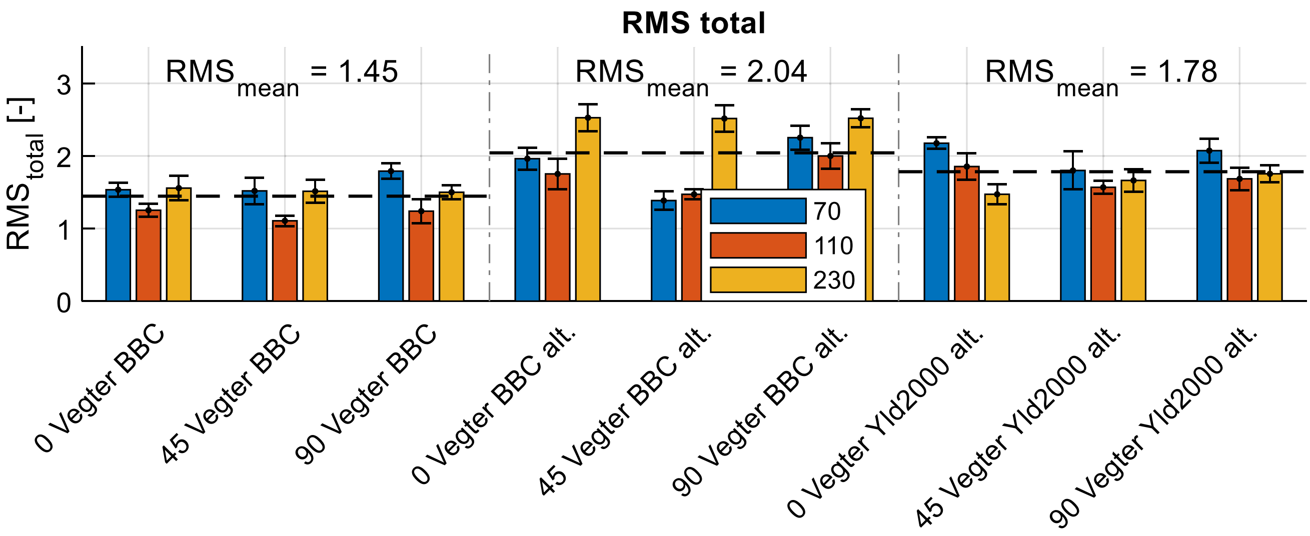

Fig. 60 Total differences between the experiments and numerical analyses for DP590HD and using the material models based on different calibration strategies their average values

Appendix

Strain distributions for material model parameter study

FSH0

Figure 61

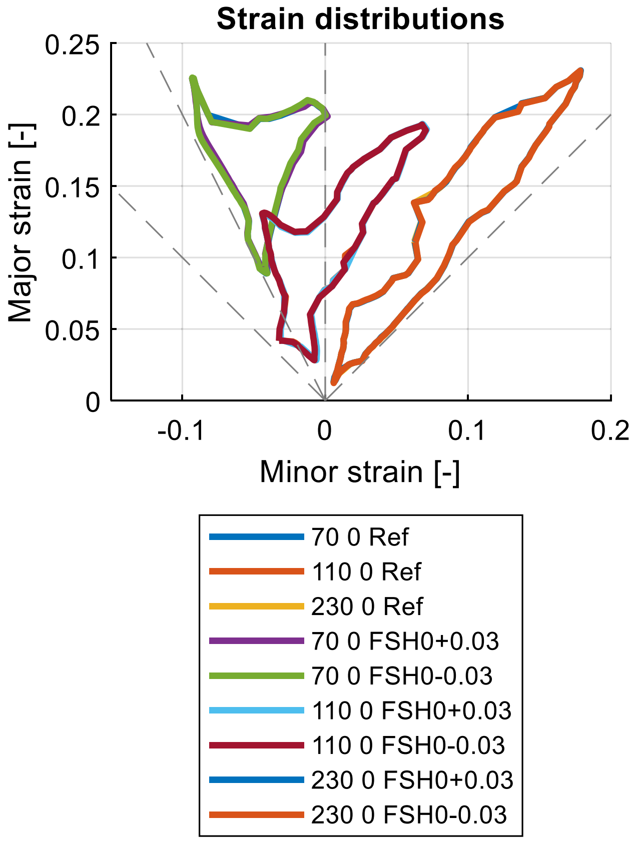

Fig. 61 Strain distributions (Sim) for parameter variations of FSH0

FUN0

Figure 62

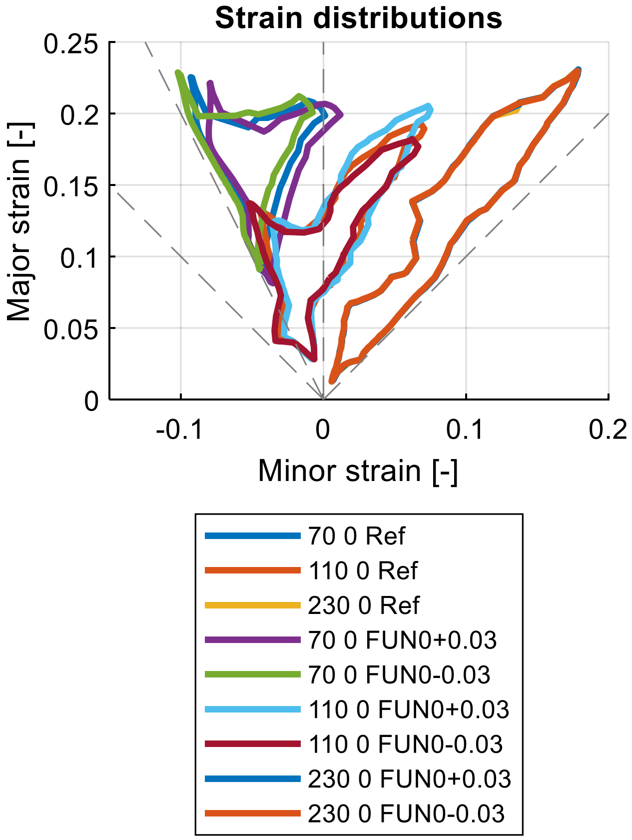

Fig. 62 Strain distributions (Sim) for parameter variations of FUN0

RUN0
Figure 63

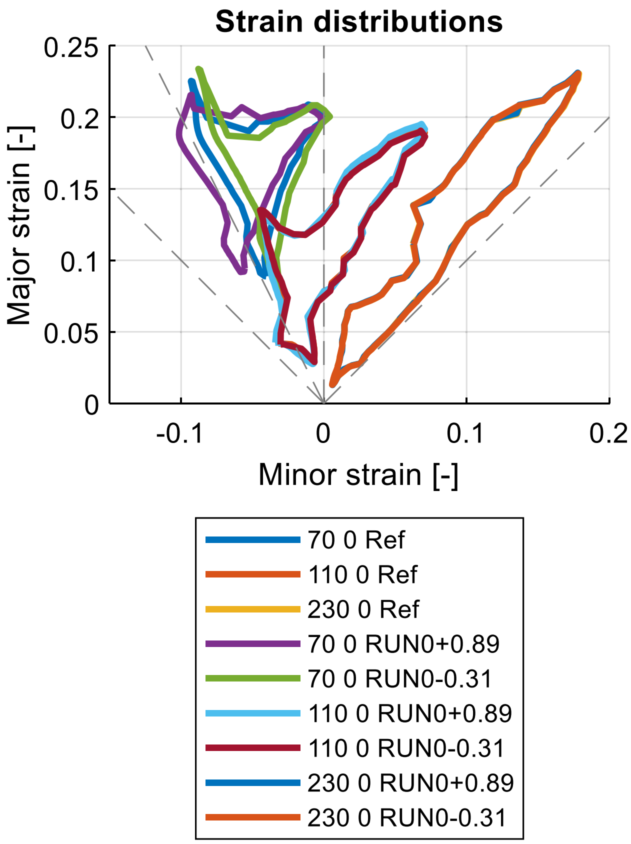

Fig. 63 Strain distributions (Sim) for parameter variations of RUN0

FPS10
Figure 64

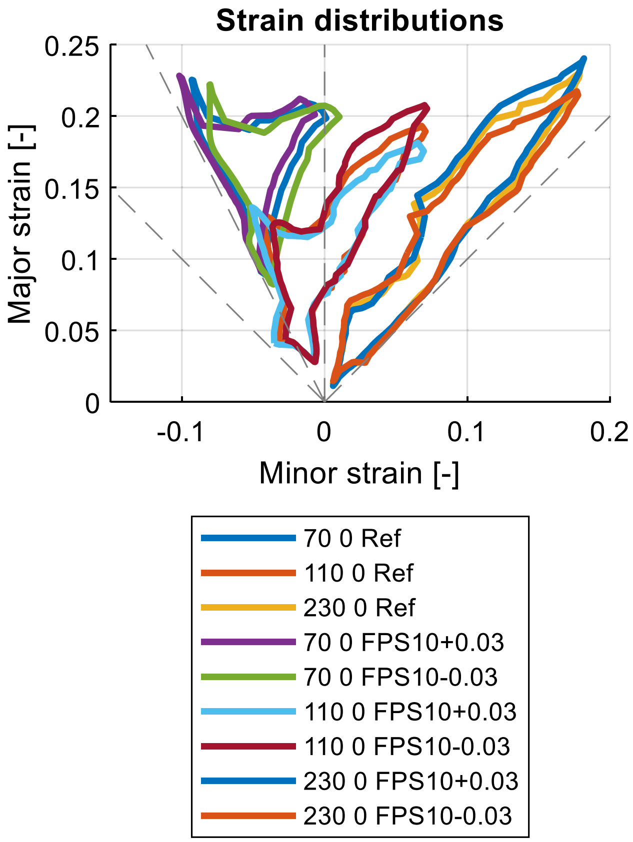

Fig. 64 Strain distributions (Sim) for parameter variations of FPS10

ALPS0
Figure 65

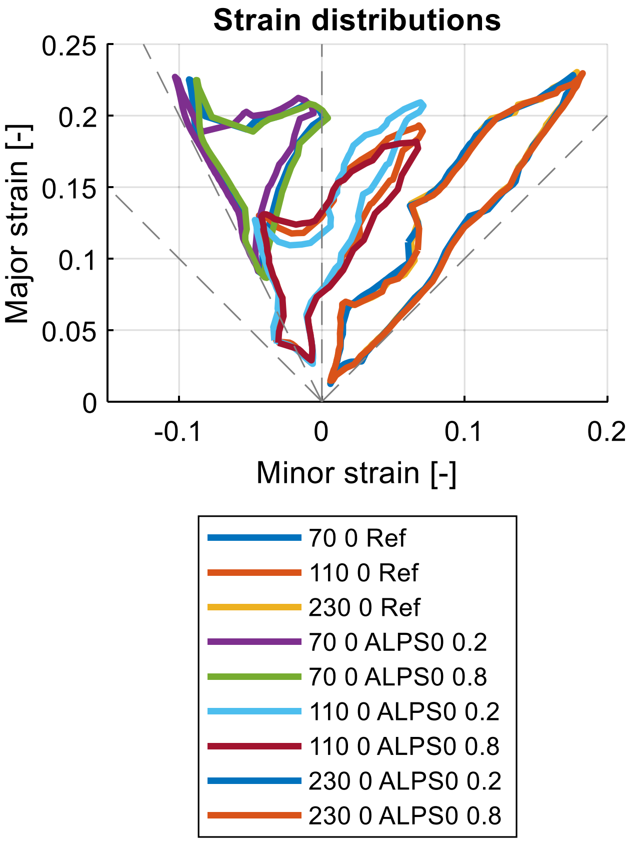

Fig. 65 Strain distributions (Sim) for parameter variations of ALPS0

FBI
Figure 66

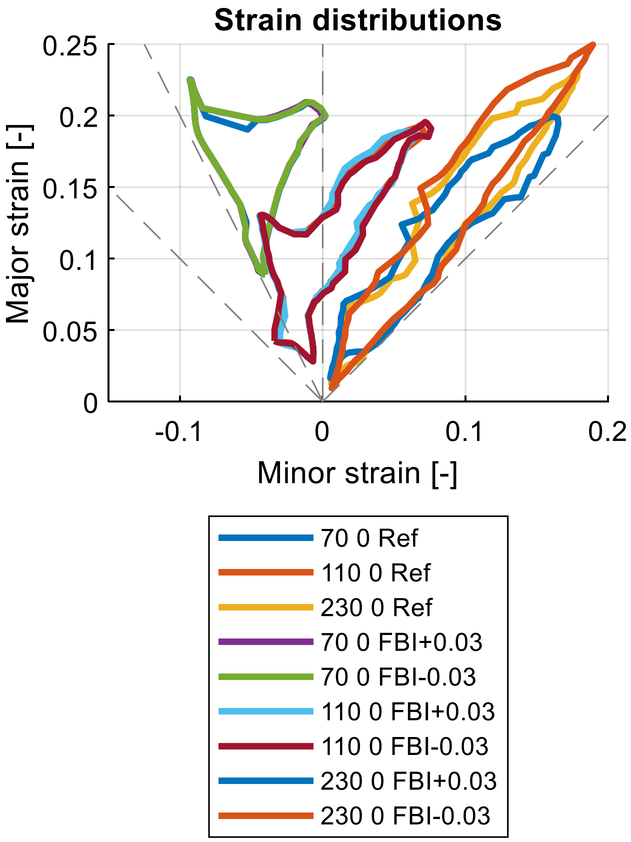

Fig. 66 Strain distributions (Sim) for parameter variations of FBI

RBI0

Figure 67

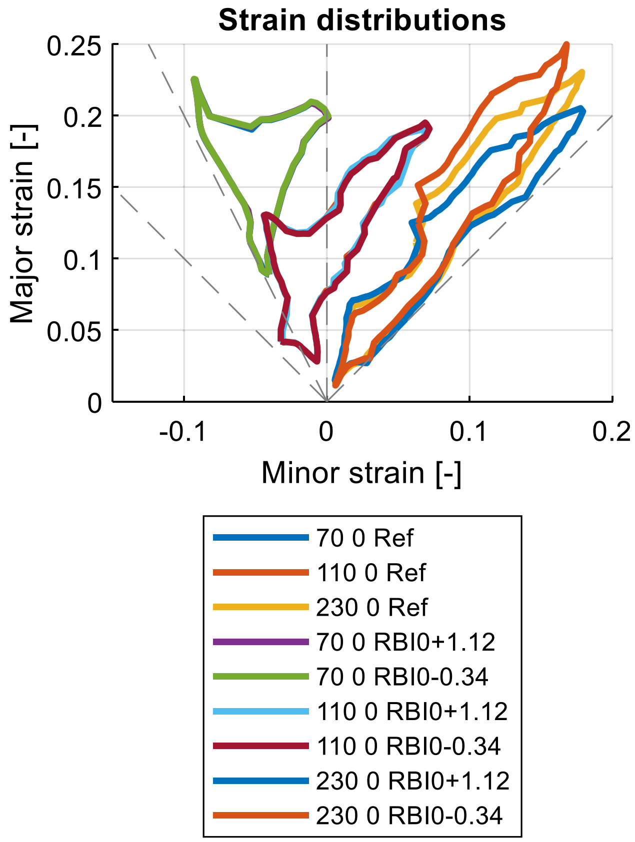

Fig. 67 Strain distributions (Sim) for parameter variations of RBI0

Yield curve ± 25 MPa

Figure 68

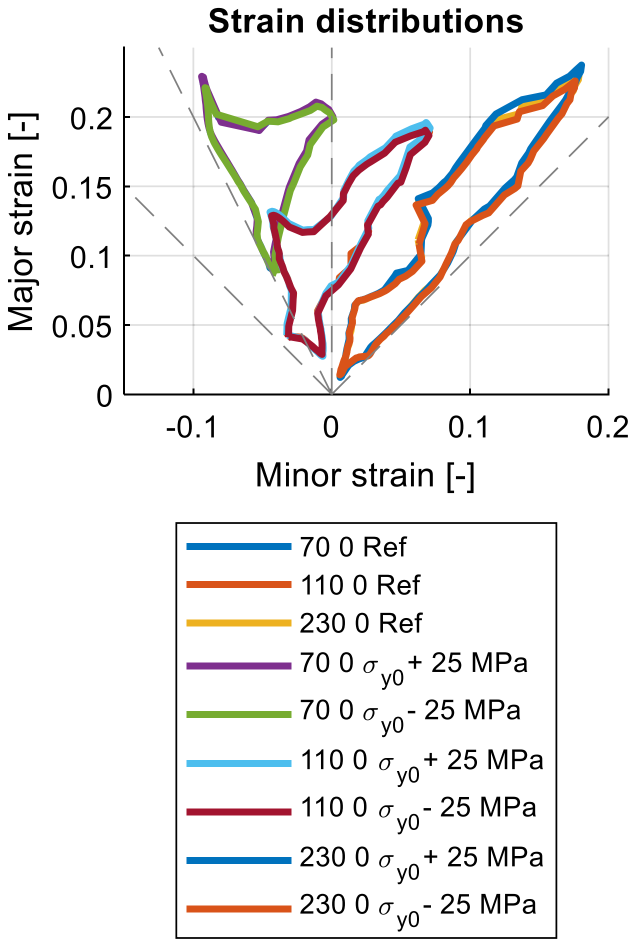

Fig. 68 Strain distributions (Sim) for different translations of the reference yield curve σ_{y0}

Yield curve steeper, flatter
Figure 69

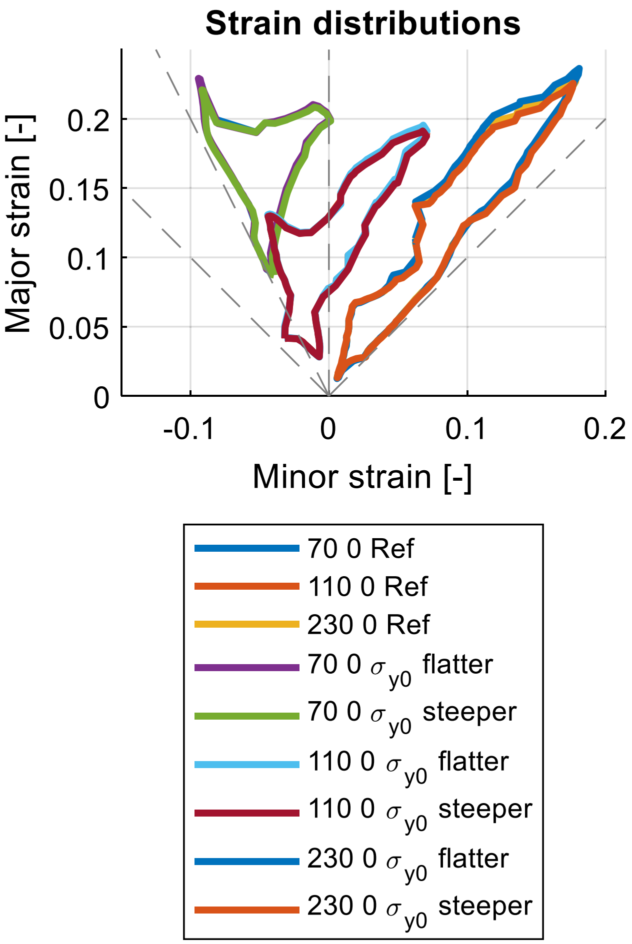

Fig. 69 Strain distributions (Sim) for different slopes of the reference yield curve σ_{y0}

Strain rate dependency parameter m
Figure 70

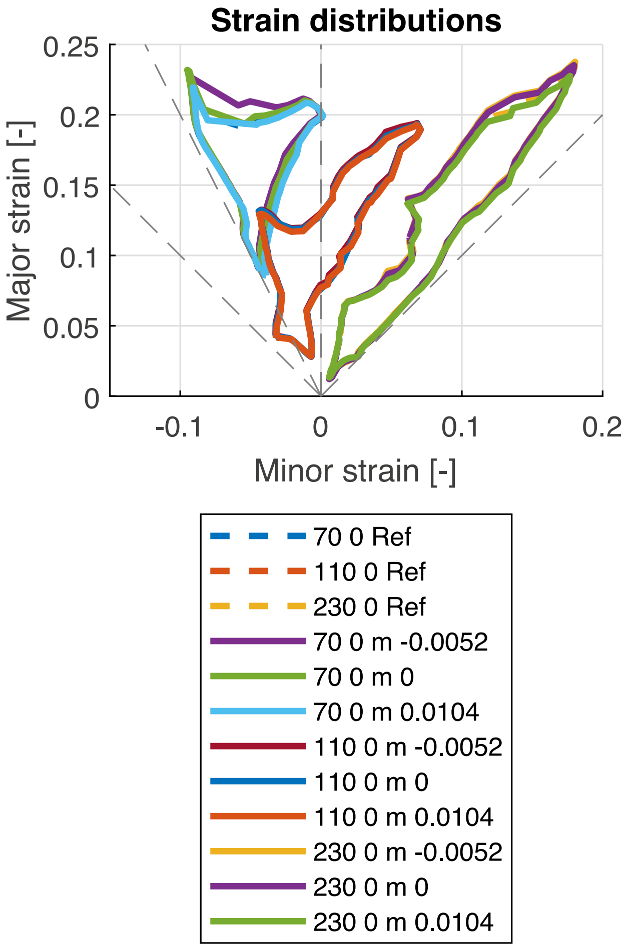

Fig. 70 Strain distributions (Sim) for parameter variations of the strain rate dependency parameter *m*

Supplementary Information The online version contains supplementary material available at https://doi.org/10.1007/s12289-022-01710-7.

Acknowledgements The authors would like to thank the German Research Foundation (Deutsche Forschungsgemeinschaft, DFG) for the financial support under the grant number 455388465. Furthermore, the authors would like to thank Martin Grünbaum and Klaus Wiegand from Mercedes-Benz AG for their valuable support.

Author contribution Not applicable.

Funding Open Access funding enabled and organized by Projekt DEAL. The authors would like to thank the German Research Foundation (Deutsche Forschungsgemeinschaft, DFG) for the financial support under the grant number 455388465.

Data availability The geometric data of the MUC-Test tool is provided as an appendix in the form of the functional surfaces.

Code availability Not applicable.

Declarations

Conflicts of interest The authors declare that they have no conflict of interest.

References

1. Ablat MA, Qattawi A (2017) Numerical simulation of sheet metal forming: a review. Int J Adv Manuf Technol 89:1235–1250. https://doi.org/10.1007/s00170-016-9103-5
2. Volk W, Groche P, Brosius A, Ghiotti A, Kinsey BL, Liewald M, Madej L, Min J, Yanagimoto J (2019) Models and modelling for process limits in metal forming. CIRP Ann 68:775–798. https://doi.org/10.1016/j.cirp.2019.05.007
3. Banabic D (2010) Sheet metal forming processes. In: Constitutive modelling and numerical simulation. Springer Berlin Heidelberg, Berlin, Heidelberg. https://doi.org/10.1007/978-3-540-88113-1
4. Bruschi S, Altan T, Banabic D, Bariani PF, Brosius A, Cao J, Ghiotti A, Khraisheh M, Merklein M, Tekkaya AE (2014) Testing and modelling of material behaviour and formability in sheet metal forming. CIRP Ann 63:727–749. https://doi.org/10.1016/j.cirp.2014.05.005
5. Manopulo N, Raemy C, Hora P (2018) A discussion of the associated flow rule based on the FAY model and Nakajima tests. J Phys Conf Ser 1063:12090. https://doi.org/10.1088/1742-6596/1063/1/012090
6. Pilthammar J, Banabic D, Sigvant M (2021) BBC05 with non-integer exponent and ambiguities in Nakajima yield surface calibration. Int J Mater Form 14:577–592. https://doi.org/10.1007/s12289-020-01545-0
7. Hippke H, Berisha B, Hora P (2020) A full-field optimization approach for iterative definition of yielding for non-quadratic and free shape yield models in plane strain. IOP Conf Ser: Mater Sci Eng 967:12084. https://doi.org/10.1088/1757-899X/967/1/012084
8. DIN EN 10027–1:2016 (2017) Designation systems for steels. Part 1: Steel names.
9. DIN EN 10027–2:2015 (2015) Designation systems for steels. Part 2: Numerical system.
10. VDA 239–100 (2016) Sheet steel for cold forming.
11. Wagoner RH (1980) Measurement and analysis of plane-strain work hardening. Metall Trans A 11:165–175. https://doi.org/10.1007/BF02700453
12. An YG, Vegter H, Elliott L (2004) A novel and simple method for the measurement of plane strain work hardening. J Mater Process Technol 155–156:1616–1622. https://doi.org/10.1016/j.jmatprotec.2004.04.344
13. Lademo OG, Engler O, Keller S, Berstad T, Pedersen KO, Hopperstad OS (2009) Identification and validation of constitutive model and fracture criterion for AlMgSi alloy with application to sheet forming. Mater Des 30:3005–3019. https://doi.org/10.1016/j.matdes.2008.12.020
14. Zhang C, Leotoing L, Zhao G, Guines D, Ragneau E (2010) A methodology for evaluating sheet formability combining the tensile test with the M-K model. Mater Sci Eng, A 528:480–485. https://doi.org/10.1016/j.msea.2010.09.001
15. Souto N, Andrade-Campos A, Thuillier S (2017) Mechanical design of a heterogeneous test for material parameters identification. Int J Mater Form 10:353–367. https://doi.org/10.1007/s12289-016-1284-9
16. Aquino J, Andrade-Campos AG, Martins JMP, Thuillier S (2019) Design of heterogeneous mechanical tests: Numerical methodology and experimental validation. Strain 55:1–18. https://doi.org/10.1111/str.12313
17. Zhang Y, Coppieters S, Gothivarekar S, van de Velde A, Debruyne D (2021) Independent Validation of Generic Specimen Design for Inverse Identification of Plastic Anisotropy. ESAFORM 2021. https://doi.org/10.25518/esaform21.2622
18. Zhang Y, van Bael A, Andrade-Campos A, Coppieters S (2022) Parameter identifiability analysis: mitigating the non-uniqueness issue in the inverse identification of an anisotropic yield function. Int J Solids Struct 111543. https://doi.org/10.1016/j.ijsolstr.2022.111543
19. Lossau S, Svendsen B (2009) Forming simulations based on parameters obtained in microstructural cold rolling simulations in comparison to conventional forming simulations. In: Proceedings of the 7th European LS-DYNA Conference. https://www.dynamore.de/en/downloads/papers/09-conference/papers/C-I-01.pdf. Accessed 17 July 2022
20. Wisselink HH, Niazi MS, Huetink J (2011) Validation of advanced material models using the crossdie test. In: 15th International Deep Drawing Research Group Conference 2011. https://iddrg.com/wp-content/uploads/2022/03/C_2_11.pdf. Accessed 17 July 2022
21. Duncombe E (1972) Plastic instability and growth of grooves and patches in plates or tubes. Int J Mech Sci 14:325–337. https://doi.org/10.1016/0020-7403(72)90087-2
22. Hill R (1948) A theory of the yielding and plastic flow of anisotropic metals. Proc R Soc A: Math Phys Eng Sci 193:281–297. https://doi.org/10.1098/rspa.1948.0045
23. Volk W, Kim JK, Suh J, Hoffmann H (2013) Anisotropic plasticity model coupled with strain dependent plastic strain and stress ratios. CIRP Ann 62:283–286. https://doi.org/10.1016/j.cirp.2013.03.055

24. Barlat F, Brem JC, Yoon JW, Chung K, Dick RE, Lege DJ, Pourboghrat F, Choi S-H, Chu E (2003) Plane stress yield function for aluminum alloy sheets—part 1: theory. Int J Plast 19:1297–1319. https://doi.org/10.1016/S0749-6419(02)00019-0
25. Banabic D, Kuwabara T, Balan T, Comsa DS, Julean D (2003) Non-quadratic yield criterion for orthotropic sheet metals under plane-stress conditions. Int J Mech Sci 45:797–811. https://doi.org/10.1016/S0020-7403(03)00139-5
26. Banabic D (2005) An improved analytical description of orthotropy in metallic sheets. Int J Plast 21:493–512. https://doi.org/10.1016/j.ijplas.2004.04.003
27. Vegter H, van den Boogaard AH (2006) A plane stress yield function for anisotropic sheet material by interpolation of biaxial stress states. Int J Plast 22:557–580. https://doi.org/10.1016/j.ijplas.2005.04.009
28. ISO 6892–1 (2019) Tensile testing - Part 1. Method of test at room temperature.
29. ISO 16808 (2014) Determination of biaxial stress-strain curve by means of bulge test with optical measuring systems.
30. Lăzărescu L, Nicodim I, Ciobanu I, Comşa DS, Banabic D (2013) Determination of material parameters of sheet metals using the hydraulic bulge test. Acta Metall Slovaca 19. https://doi.org/10.12776/ams.v19i1.81
31. Mulder J, Vegter H, Aretz H, Keller S, van den Boogaard AH (2015) Accurate determination of flow curves using the bulge test with optical measuring systems. J Mater Process Technol 226:169–187. https://doi.org/10.1016/j.jmatprotec.2015.06.034
32. Merklein M, Kuppert A (2009) A method for the layer compression test considering the anisotropic material behavior. Int J Mater Form 2:483–486. https://doi.org/10.1007/s12289-009-0592-8
33. Flores P, Tuninetti V, Gilles G, Gonry P, Duchêne L, Habraken AM (2010) Accurate stress computation in plane strain tensile tests for sheet metal using experimental data. J Mater Process Technol 210:1772–1779. https://doi.org/10.1016/j.jmatprotec.2010.06.008
34. ISO 10113:2020 (2020) Metallic materials - Sheet and strip - Determination of plastic strain ratio.
35. Benkert T, Hartmann C, Eder M, Speckmaier F, Volk W (2019) MaterialModeler - From experimental raw data to a material model. SoftwareX 10:100249. https://doi.org/10.1016/j.softx.2019.100249
36. Logan RW, Hosford WF (1980) Upper-bound anisotropic yield locus calculations assuming <111> -pencil glide. Int J Mech Sci 22:419–430. https://doi.org/10.1016/0020-7403(80)90011-9
37. ANSI H 35.1/H 35.1M (2017) Standard Alloy and Temper Designation Systems for Aluminum.
38. DIN 1725–1:1983 (1983) Aluminium alloys; Wrought alloys.
39. ASTM E 527 (2016) Standard Practice for Numbering Metals and Alloys in the Unified Numbering System (UNS).
40. EN 573–2:1994 (1994) Aluminium and aluminium alloys - Chemical composition and form of wrought products. Part 2: Chemical symbol based designation system.
41. Eder M, Gruber M, Manopulo N, Volk W (2021) Potentials for material card validation using an innovative tool. IOP Conf Ser: Mater Sci Eng 1157:12067. https://doi.org/10.1088/1757-899X/1157/1/012067
42. ISO 12004–2 (2021) Determination of forming-limit curves - Part 2: Determination of forming-limit curves in the laboratory.
43. Felippa CA (2004) Introduction to Finite Element Methods. Material assembled from Lecture Notes for the course Introduction to Finite Elements Methods (ASEN 5007) offered from 1986 to date at the Aerospace Engineering Sciences Department of the University of Colorado at Boulder. Last updated Fall 2004, Boulder, Colorado, USA
44. Yang K-H (ed) (2018) Basic finite element method as applied to injury biomechanics. Academic Press, Amsterdam
45. Courant R, Friedrichs K, Lewy H (1928) Über die partiellen Differenzengleichungen der mathematischen. Physik Math Ann 100:32–74. https://doi.org/10.1007/BF01448839
46. DYNAmore: LS-DYNA User's Guide. Time step size. https://www.dynasupport.com/tutorial/ls-dyna-users-guide/time-step-size. Accessed 08 Mar 2022